Applications in Engineering Science 7 (2021) 100065

Contents lists available at ScienceDirect

Applications in Engineering Science

journal homepage: www.sciencedirect.com/journal/applications-in-engineering-science

Modeling cyclic plasticity of additively manufactured alloy Mar-M-509 using a high-performance spectral-based micromechanical model

Adnan Eghtesad, Marko Knezevic *

Department of Mechanical Engineering, University of New Hampshire, 33 Academic Way, Kingsbury Hall, W119, Durham, NH 03824, USA

ARTICLE INFO

Keywords:
Microstructures
Dislocation density
Crystal plasticity
Additive manufacturing
Mar-M-509

ABSTRACT

A high-performance full-field spectral crystal plasticity model referred to as MPI-ACC-EVPCUFFT is adapted to study the deformation behavior of additively manufactured Mar-M-509® cobalt-based superalloy. The model features a dislocation density-based hardening law for the evolution of slip resistance, a barrier effect induced by grain morphology to influence the slip resistance, and a slip system-level back-stress law for adjusting the driving force to slip. The model is used to interpret and predict strength of the alloy in tension, compression, load reversal, and low-cycle fatigue as a function of initial microstructure. The initial microstructure varied from sample-to-sample to represent the effects of build orientation and heat treatment. Results show that the model successfully reproduces phenomena pertaining to monotonic and cyclic deformation including the non-linear unloading, Bauschinger effect, and cyclic hardening/softening using a single set of model parameters. Moreover, the model offers insights into fluctuations of mechanical fields and strain partitioning.

1. Introduction

Metallic alloys as polycrystalline materials exhibit anisotropy owing to their microstructures, and especially, to their non-random distribution of crystal lattice orientations (Fuentes-Cobas et al., 2013; Cantara et al., 2019). While phenomenological models based on continuum plasticity are extensively used in simulations of metal plasticity, lacking the ability in predicting the anisotropy at a single-crystal level classifies multiscale constitutive laws such as those based on the crystal plasticity theory as more favorable. Several crystal plasticity-based homogenizations are well established to link the microstructural response of the material with its overall structural properties. Such models have been evolved significantly in the course of last few decades from Taylor-type upper bound models (Knezevic et al., 2008; Taylor, 1938; Van Houtte et al., 2004; Knezevic et al., 2009; Knezevic and Savage, 2014; Knezevic and Kalidindi, 2017; Knezevic and Kalidindi, 2007) to mean-field self-consistent models (Lebensohn et al., 2007; Zecevic et al., 2015; Lebensohn and Tomé, 1993; Knezevic et al., 2016; Knezevic et al., 2015; Knezevic et al., 2014; Zecevic et al., 2018; Zecevic et al., 2019). While these models are computationally efficient, they lack the ability to explicitly model microstructures and constituent grains, and therefore, are unable to provide qualification and quantification of micromechanical fields as a consequence of grain-to-grain interactions. To account for such interactions, full-field crystal plasticity models have been developed (Lebensohn, 2001; Kalidindi et al., 1992; Ardeljan et al., 2017; Ardeljan et al., 2016; Ardeljan and Knezevic, 2018; Ardeljan et al., 2015; Feather et al., 2020; Feather et al., 2021; Feather et al., 2019; Zecevic et al., 2015; Zecevic et al., 2015). Of particular interest in the present work is the full-field elasto-visco plastic fast Fourier transform (EVPFFT) model, which has recently been cast into a high-performance parallel implementation (Eghtesad et al., 2020). The model is adapted here to study the deformation behavior of additively manufactured Mar-M-509® (MM509) cobalt-based superalloy.

Superalloys are known for their oxidation/corrosion resistance and high strength at high temperatures including creep (Akande et al., 2021). Superalloys fall into four different categories, nickel based (Ni), nickel-iron based (Ni-Fe), cobalt based (Co), and nickel-cobalt based (Ni-Co) (Li et al., 2020; Ding et al., 2020; Zhang et al., 2020; Xu et al., 2020; Wang et al., 2020; Zhang et al., 2020; Tamura et al., 2021). These categories differ in their structural properties under high-temperature conditions. For example, Co-based superalloys are better for hot-corrosion resistance compared to Ni-based superalloys. The excellent corrosion resistance of Co-based alloys is discussed in Galiullin et al. (2019) and Lashgari et al. (2021). This makes them excellent materials for long-lived metallic components, which experience stresses at very high temperatures. The common application for superalloys

* Corresponding author.
E-mail address: marko.knezevic@unh.edu (M. Knezevic).

https://doi.org/10.1016/j.apples.2021.100065
Received 18 June 2021; Received in revised form 8 August 2021; Accepted 11 August 2021
Available online 13 August 2021

owing to their exceptional material properties is in turbomachinery, aircraft jet engines, and oil industry (Bišs, 1977; Davis, 1997; Koenigsmann et al., 2016; Uhlig et al., 2017; Knezevic et al., 2012; Thellaputta et al., 2017). Such parts often have complex geometries. Co-based superalloys are usually cast and then machined to meet specification. In addition, the material is often subjected to other thermo-mechanical treatments. The machining is costly due to their high strength/hardness. Co-based alloys can be created by additive manufacturing (AM). A few studies on the effects of AM on the microstructure and mechanical properties for such alloys exist in the literature (Chen et al., 2017; Cloots et al., 2016; Kaschel et al., 2020), while more studies exist on such cast alloys (Biss, 1977; Drapier et al., 1968; Whittenberger, 1981). The AM works studied in particular the effect of process parameters on microstructure in as-built Co-based superalloys such as MM509. Depending on the manufactured component size, AM can reduce the need for machining due to its ability to make end-use components of complex geometries (Murr et al., 2009; Santos et al., 2006; Herderick, 2015; Frazier, 2014; Gong and Manogharan, 2020). Moreover, AM has proven effective for restoring features in damaged parts (Safdar et al., 2013; Perini et al., 2020). The performances of AM synthesized materials are being increasingly evaluated (Chen et al., 2017; Cloots et al., 2016; Gribbin et al., 2019; Knezevic and Ghorbanpour, 2018; Bronkhorst et al., 2019; Ghorbanpour et al., 2017; Ferreri et al., 2020; Ferreri et al., 2020; Ferreri et al., 2020).

Effects of build orientation and heat treatment on the evolution of microstructure and mechanical properties of alloy MM509 created via laser powder bed fusion have recently been studied in (Ferreri et al., 2019). Samples were produces in the as-built condition and several heat-treated (HT) conditions to possibly increase the alloy ductility. Strength of the alloy was found to be a strong function of build orientation in the as-build condition, while the alloy was softer and more ductile after HT due to microstructural changes and the evolution of internal stresses. Such characteristics were rationalized by microstructural characterization. Grain structure, texture, and % recrystallization were measured using electron backscattered diffraction (EBSD).

While comprehensive experimental and numerical studies have been conducted into deformation behavior of INC718 Ni-based superalloys (Cruzado et al., 2017; Ghorbanpour et al., 2017; Cruzado et al., 2018; Tao et al., 2019; Kergaßner et al., 2018; Huang et al., 2020; Feng et al., 2017), less attentions is dedicated to Co-based alloys (Knezevic et al., 2014). To the authors' knowledge, there are no computer simulations studying the micromechanical response of alloy MM509 in the current literature. This work attempts to model and interpret the alloy behavior using crystal plasticity modeling. The particular model used in the work is the EVPFFT model (Lebensohn et al., 2012; Eghtesad et al., 2018) accelerated on multiple central processing units (CPUs) and graphics processing units (GPUs) (Eghtesad et al., 2020; Eghtesad and Knezevic, 2020; Eghtesad et al., 2018). The model features a dislocation density-based hardening law for the evolution of slip resistance, a barrier effect induced by grain morphology to influence the slip resistance, and a slip system-level back-stress law for adjusting the driving force to slip. The model is utilized to study monotonic, load reversal, and cyclic behavior of the alloy at different cyclic strain amplitudes as a function of initial microstructures created via AM and subsequent HT. Changes in grain structure, crystallographic texture, and fraction of recrystallized regions in the microstructure as a consequence of HT are explicitly modeled. Moreover, the initial dislocation density is adjusted to reflect recrystallized versus not recrystallized grains while reproducing the mechanical data. The effective and micromechanical responses of the alloy in different conditions are computed through simulations of voxel-based microstructural cells. The cells consistent with the measured microstructures are constructed synthetically in Dream.3d (Groeber and Jackson, 2014; Barrett et al., 2019; Eghtesad et al., 2018) to initialize the model setups for the simulations. In doing so, statistics of the experimentally measured microstructural features including grain size/shape, texture, and % recrystallized are input into the software. Strength is predicted as a function of microstructure and various loading scenarios including low-cycle fatigue (LCF) using the model. Modeling framework, simulation setups, results, and insights from the results are presented and discussed in this paper.

2. Modeling framework

Green's function-based EVPFFT models (Lebensohn, 2001; Eghtesad et al., 2018; Eghtesad et al., 2018; Knezevic et al., 2016) are aimed at predicting mechanical fields and mechanical response of polycrystalline metals. These models are more computationally efficient than crystal plasticity finite element method (CPFEM) models (Beaudoin et al., 1994; Ardeljan et al., 2014; Knezevic et al., 2014; Knezevic et al., 2010; Kalidindi et al., 2006; Ardeljan et al., 2016; Barrett et al., 2020; Barrett et al., 2018; Barrett and Knezevic, 2019) due to the repetitive use of the efficient FFT algorithms, which avoid the time-consuming inversion of large matrices, needed in CPFEM. Recently, the parallel versions of the code running on distributed nodes of central processing units (CPUs) (Eghtesad et al., 2018) and graphics processing units (GPU) (Eghtesad et al., 2020; Eghtesad et al., 2018) (multi-GPU) have offered further speed ups relying on specialized computer hardware. As a result, simulations of high-resolution microstructures can be performed in a reasonable time. In this work, the multi-GPU version of the EVPFFT solver, MPI-ACC-EVPCUFFT, further developed for alloy Inconel 718 (Zong and Wu, 2017), is adapted here to simulate and interpret the behavior of alloy MM509 under several loading scenarios including LCF. In the notation we use, tensors are denoted by non-italic bold letters while scalars and tensor components are italic and not bold. To denote a contracted or dot product and uncontracted or tensor product, $\cdot$and $\otimes$ are used, respectively.

In what follows, we elaborate on the governing equations of the EVPFFT micromechanical solver. We define the crystal plasticity power-law equation correlating the plastic strain rate and crystal stress, followed by an elasto-plastic decomposition leveraging the Hooks's law. Subsequently, we describe the full-field solution procedure utilizing FFTs and Green's theory. In particular, the iterative Newton-Raphson (NR) procedures for obtaining the crystal stresses and for obtaining the field equilibrium upon homogenization are described. Finally, we summarize a physics-based dislocation density hardening law for capturing the flow behavior of the material and a kinematic hardening back-stress law at the slip-system level for capturing nonlinear unloading and the Bauschinger effect upon load reversal.

In the crystal visco-plasticity, strain rate, $\dot{\boldsymbol{\varepsilon}}^p(\mathbf{x})$, and Cauchy stress, $\boldsymbol{\sigma}(\mathbf{x})$, are related at any spatial material point x through a sum of shears on available slip systems, N, using (Hutchinson, 1976; Asaro and Needleman, 1985)

$$\dot{\boldsymbol{\varepsilon}}^p(\mathbf{x}) = \sum_{s=1}^{N} \mathbf{P}^s(\mathbf{x})\,\dot{\gamma}^s(\mathbf{x}) = \dot{\gamma}_0 \sum_{s=1}^{N} \mathbf{P}^s(\mathbf{x}) \left(\frac{\mathbf{P}^s(\mathbf{x}) \cdot \boldsymbol{\sigma}(\mathbf{x}) - \tau_{bs}{}^s(\mathbf{x})}{\tau_c{}^s(\mathbf{x})} \right)^n, \tag{1a}$$

$$\mathbf{P}^s_{sc} = \frac{1}{2}(\mathbf{b}^s \otimes \mathbf{n}^s + \mathbf{n}^s \otimes \mathbf{b}^s), \tag{1b}$$

$$\mathbf{P}_{ns}{}^s = c_1(\mathbf{t}^s \otimes \mathbf{b}^s) + c_2(\mathbf{t}^s \otimes \mathbf{n}^s) + c_3(\mathbf{n}^s \otimes \mathbf{n}^s) + c_4(\mathbf{t}^s \otimes \mathbf{t}^s) - (c_3 + c_4)(\mathbf{b}^s \otimes \mathbf{b}^s), \tag{1c}$$

$$\mathbf{P}^s = \mathbf{P}^s_{sc} + \mathbf{P}^s_{ns}. \tag{1d}$$

In Eq. (1a), $\dot{\gamma}^s$ and $\tau_c{}^s$are the shearing rate and the slip resistance, respectively. The parameter $\dot{\gamma}_0$ is a reference shearing rate (0.001 /s) and n is the power-law visco-plastic exponent (20). The value of 20 ensures proper selection of active slip systems. The term $\tau_{bs}{}^s(\mathbf{x})$ is the slip system back-stress influencing the driving force to slip. The Burgers vector $\mathbf{b}^s$ and the slip system normal $\mathbf{n}^s$ with $\mathbf{t}^s = \mathbf{b}^s \times \mathbf{n}^s$ define the geometry of slip system, s. The face centered cubic (FCC) structure of MM509

deforms using $\{110\}\langle\bar{1}11\rangle$ family of slip systems. 12 positive s+ and 12 negative s- directions are considered by the model. In addition to stress projected on the glide plane and in the glide direction, two orthogonal shear stress components and the three normal stress components are included in the activation criterion (Savage et al., 2017) (non-Schmid effects). The non-Schmid coefficients c_1, c_2, c_3, c_4 weight the stress contributions.

Hooke's law is used as the constitutive relation between stress and strain

$$\boldsymbol{\sigma}^{t+\Delta t}(\mathbf{x}) = \mathbf{C}(\mathbf{x})\,\boldsymbol{\varepsilon}^{e,t+\Delta t}(\mathbf{x}) = \mathbf{C}(\mathbf{x})\,(\boldsymbol{\varepsilon}^{t+\Delta t}(\mathbf{x}) - \boldsymbol{\varepsilon}^{p,t}(\mathbf{x}) - \dot{\boldsymbol{\varepsilon}}^{p,t+\Delta t}(\mathbf{x},\boldsymbol{\sigma}^{t+\Delta t})\Delta t), \tag{2}$$

where $\boldsymbol{\sigma}(\mathbf{x})$is the Cauchy stress, $\mathbf{C}(\mathbf{x})$ is the elastic stiffness obtained from the crystal elastic constants, and $\boldsymbol{\varepsilon}(\mathbf{x})$,$\boldsymbol{\varepsilon}^e(\mathbf{x})$, and $\boldsymbol{\varepsilon}^p(\mathbf{x})$ are the total, elastic, and plastic strains. From Eq. (2), the total strain is

$$\varepsilon^{t+\Delta t}(\mathbf{x}) = \mathbf{C}^{-1}(\mathbf{x})\,\sigma^{t+\Delta t}(\mathbf{x}) + \varepsilon^{p,t}(\mathbf{x}) + \dot{\varepsilon}^{p,t+\Delta t}(\mathbf{x},\sigma^{t+\Delta t})\Delta t. \tag{3}$$

2.1. Full-field solution utilizing FFTs and Green's theory

After adding and subtracting the stiffness of a reference linear medium, $\mathbf{C}^0$, multiplied by the displacement gradient, $u_{k,l}(\mathbf{x})$, from the Cauchy stress, we obtain

$$\sigma_{ij}(\mathbf{x}) = \sigma_{ij}(\mathbf{x}) + C^0{}_{ijkl}u_{k,l}(\mathbf{x}) - C^0{}_{ijkl}u_{k,l}(\mathbf{x}), \tag{4}$$

Furthermore, we can write

$$\sigma_{ij}(\mathbf{x}) = C^0{}_{ijkl}u_{k,l}(\mathbf{x}) + \phi_{ij}(\mathbf{x}), \tag{5}$$

with

$$\phi_{ij}(\mathbf{x}) = \sigma_{ij}(\mathbf{x}) - C^0{}_{ijkl}u_{k,l}(\mathbf{x}), \tag{6}$$

where the term $\phi_{ij}(\mathbf{x})$ represents the polarization field. Using the equilibrium equation,$\sigma_{ij,j}(\mathbf{x}) = 0$, Eq. (5) is

$$C^0{}_{ijkl}u_{k,lj}(\mathbf{x}) + \phi_{ij,j}(\mathbf{x}) = 0. \tag{7}$$

Relying on Green's approach to solve partial differential equations (Bellman and Adomian, 1985), Green's function $G_{km}(\mathbf{x})$ is associated to the displacement field $u_k(\mathbf{x})$ as

$$C^0{}_{ijkl}G_{km,lj}(\mathbf{x}-\mathbf{x}') + \delta_{im}\delta(\mathbf{x}-\mathbf{x}') = 0. \tag{8}$$

The convolution theorem (Zayed, 1998) is then used to obtain the local displacement gradient fluctuation tensor

$$\widetilde{u}_{k,l}(\mathbf{x}) = \int_{R^3} G_{ki,jl}(\mathbf{x}-\mathbf{x}')\phi_{ij}(\mathbf{x}')\,d\mathbf{x}'. \tag{9}$$

The strain field around the average strain value, E_{ij}, is then

$$\varepsilon_{ij}(\mathbf{x}) = E_{ij} + FT^{-1}\left(sym\left(\widehat{\Gamma}^0{}_{ijkl}(\mathbf{k})\right)\widehat{\phi}_{kl}(\mathbf{k})\right), \tag{10}$$

where the symbols FT^{-1} and "∧" mean inverse Fourier transforms and direct Fourier transform, respectively. $\mathbf{k}$ is a point (frequency) in Fourier Space. The tensor $\widehat{\Gamma}^0{}_{ijkl}(\mathbf{k})$ is

$$\widehat{\Gamma}^0{}_{ijkl}(\mathbf{k}) = -k_j k_l \widehat{G}_{ik}(\mathbf{k}),\ \widehat{G}_{ik}(\mathbf{k}) = \left[C_{kjil}k_l k_j\right]^{-1}. \tag{11}$$

An iterative procedure is used to obtain a solution for Eq. (7). If we consider $e_{ij}{}^{(i)}$ and $\lambda_{ij}{}^{(i)}$to be an initial guess for the strain and stress fields, respectively, we get from Eq. (6)

$$\phi_{ij}{}^{(i)}(\mathbf{x}) = \lambda_{ij}{}^{(i)}(\mathbf{x}) - C^0{}_{ijkl}e_{kl}{}^{(i)}(\mathbf{x}), \tag{12}$$

Eq. (10) is then used for the next guess for the strain field

$$e_{ij}{}^{(i+1)}(\mathbf{x}) = E_{ij} + FT^{-1}\left(sym\left(\widehat{\Gamma}^0{}_{ijkl}(\mathbf{k})\right)\widehat{\phi}^{(i)}{}_{kl}(\mathbf{k})\right). \tag{13}$$

To use the stress directly rather than the polarization, Eq. (13) is rewritten as (Michel et al., 2001)

$$e_{ij}^{(i+1)}(\mathbf{x}) = E_{ij} + FT^{-1}\left(\widehat{\widehat{e}}_{ij}^{(i+1)} + sym\left(\widehat{\Gamma}^o_{ijkl}(\mathbf{k})\widehat{\lambda}^{(i)}_{kl}(\mathbf{k})\right)\right) \tag{14}$$

An augmented Lagrangian scheme is used (Lebensohn et al., 2012) to minimize the residual as a function of the stress, $\boldsymbol{\sigma}^{(i+1)}$, and strain, $\boldsymbol{\varepsilon}^{(i+1)}$

$$R_k\left(\boldsymbol{\sigma}^{(i+1)}\right) = \sigma_k{}^{(i+1)} + C_{kl}{}^0\varepsilon_l{}^{(i+1)}\left(\boldsymbol{\sigma}^{(i+1)}\right) - \lambda_k{}^{(i)} - C_{kl}{}^0 e_l{}^{(i+1)}, \tag{15}$$

In the above equation, the Voigt notation is used for the symmetric tensors $\sigma_{ij}$and C_{ijkl} as

$$\begin{aligned}&\sigma_{ij}\rightarrow\sigma_k, k = 1,6\\ &C_{ijkl}\rightarrow C_{kl}, k, l = 1,6.\end{aligned} \tag{16}$$

Eq. (15) is solved using the Newton's method as

$$\sigma_k{}^{(i+1,j+1)} = \sigma_k{}^{(i+1,j)} - \left(\frac{\partial R_k}{\partial\sigma_l}|_{\boldsymbol{\sigma}^{(i+1,j)}}\right)^{-1} R_l\left(\boldsymbol{\sigma}^{(i+1,j)}\right), \tag{17}$$

where $\sigma_k{}^{(i+1,j+1)}$is the (j+1) trial for stress field $\sigma_k{}^{(i+1)}$. Note that "j" enumerates the NR stress iterations, while "i" enumerates the field equilibrium iterations. Using Eq. (3), the Jacobian is

$$\frac{\partial R_k}{\partial\sigma_l}|_{\boldsymbol{\sigma}^{(i+1,j)}} = \delta_{kl} + C_{kq}{}^0 C_{ql}{}^{-1} + \Delta t C_{kq}{}^0\frac{\partial\dot{\varepsilon}_q{}^p}{\partial\sigma_l}|_{\boldsymbol{\sigma}^{(i+1,j)}}. \tag{18}$$

The term $\frac{\partial\dot{\varepsilon}_q{}^p}{\partial\sigma_l}|_{\boldsymbol{\sigma}^{(i+1,j)}}$ is

$$\frac{\partial\dot{\varepsilon}_q{}^p}{\partial\sigma_l}|_{\boldsymbol{\sigma}^{(i+1,j)}} \cong n\dot{\gamma}_0\sum\nolimits_{s=1}^{N}\frac{P^s{}_q P^s{}_l}{\tau_c{}^s(\boldsymbol{\sigma}^{(i+1,j)}(\mathbf{x}))}\left(\frac{\mathbf{P}^s(\mathbf{x})\cdot\boldsymbol{\sigma}(\mathbf{x}) - \tau_{bs}{}^s}{\tau_c{}^s(\boldsymbol{\sigma}^{(i+1,j)}(\mathbf{x}))}\right)^{n-1}. \tag{19}$$

Incorporating Eq. (19) into Eq. (18) gives

$$\begin{aligned}\frac{\partial R_k}{\partial\sigma_l}|_{\boldsymbol{\sigma}^{(i+1,j)}} \cong\ &\delta_{kl} + C_{kq}{}^0 C_{ql}{}^{-1}\\ &+ \left(\Delta t\, n\dot{\gamma}_0\right)C_{kq}{}^0\sum\nolimits_{s=1}^{N}\frac{P^s{}_q P^s{}_l}{\tau_c{}^s(\boldsymbol{\sigma}^{(i+1,j)}(\mathbf{x}))}\left(\frac{\mathbf{P}^s(\mathbf{x})\cdot\boldsymbol{\sigma}(\mathbf{x}) - \tau_{bs}{}^s}{\tau_c{}^s(\boldsymbol{\sigma}^{(i+1,j)}(\mathbf{x}))}\right)^{n-1}.\end{aligned} \tag{20}$$

Minimizing the residual $R_k$by the Newton's iterations, the solution for stress is obtained at each FFT point as the next trial for Eqs. (12) and (14). The procedure continues until the convergence to TOL_{NR} is reached for each crystal stress

$$\frac{(\sigma_k{}^{(i+1,j+1)} - \sigma_k{}^{(i+1,j)})(\sigma_k{}^{(i+1,j+1)} - \sigma_k{}^{(i+1,j)})}{\sqrt{\lambda_{ij}{}^{(i)}\lambda_{ij}{}^{(i)}}} \prec TOL_{NR} = 10^{-6}. \tag{21}$$

Given the exponent n and the tolerance, the total number of iterations for stress is in the range from 3 to 6, which is about the same as in the original code (Lebensohn et al., 2012).

The stress and strain field tolerances (TOL_{stress_field} , TOL_{strain_field}) after solving Eq. (15) are

$$\frac{\left\langle\left(\sigma_k^{(i+1)} - \lambda_k^{(i)}\right)\left(\sigma_k^{(i+1)} - \lambda_k^{(i)}\right)\right\rangle}{\sqrt{\frac{3}{2}\Sigma'_{ij}{}^{(i)}\Sigma'^{(i)}_{ij}}} \prec TOL_{stress\_field} = 10^{-6}) \tag{22a}$$

$$\frac{\left\langle(\varepsilon_k^{(i+1)} - e_k^{(i)})(\varepsilon_k^{(i+1)} - e_k^{(i)})\right\rangle}{\sqrt{\frac{2}{3}E'_{ij}{}^{(i)}E'^{(i)}_{ij}}} \prec TOL_{strain\_field} = 10^{-6} \tag{22b}$$

where $\langle\rangle$ represents the volume average. Tensors Σ'_{ij} and E'_{ij} are the

deviatoric stress and plastic strain of the polycsrystal obtained by averaging such local quantities

$$\Sigma'_{ij} = \frac{\sum_{X,Y,Z}\left(\sigma'_{ij}(\mathbf{x})\right)}{N_1 \times N_2 \times N_3} \;;\; N_1, N_2, N_3 = \#of\ voxels\ in\ X, Y, Z,$$
$$E'_{ij} = \frac{\sum_{X,Y,Z}\left(\varepsilon^{p}_{ij}(\mathbf{x})\right)}{N_1 \times N_2 \times N_3}. \tag{23}$$

The total number of iterations for obtaining the field solution is about 20 for the selected tolerances, which is consistent with the original unmodified code (Lebensohn et al., 2012).

2.2. Hardening law in MPI-ACC-EVPCUFFT

The model incorporates a dislocation density (DD)-based hardening law (Eghtesad and Knezevic, 2020; Zong and Wu, 2017; Zecevic et al., 2018; Zecevic et al., 2020). The content of dislocation density evolves as the material is deformed plastically. The rate of evolution is a thermally activated process, which is dependent on temperature and on strain rate. In the description that follows, s and s' denote the slip systems. The evolution of slip resistance per slip system incorporates three terms

$$\tau^s_c = \tau^s_0 + \tau^s_{forest} + \tau_{deb}. \tag{24a}$$

The first term, τ^s_0, is the initial value that does not evolve and consists of three terms

$$\tau^s_0 = \tau_0 + \tau^s_{0,HP} + \tau_{0,forest}, \tag{24b}$$

where τ_0 is the frictional term embedding the effects of solid solution and carbides, $\tau^s_{0,HP}$is the barrier contribution term, and $\tau_{0,forest}$ is the term reflecting the initial forest dislocation density content. The barrier term captures the grain shape and size induced microstructural anisotropy using (Beyerlein and Tomé, 2008)

$$\tau^s_{0,HP} = \frac{H\mu^{MM509}\sqrt{b^{MM509}}}{\sqrt{d^s_{mfp}}}, \tag{25a}$$

$$d^s_{mfp} = \frac{2}{\sqrt{\left(\frac{\tilde{b}^s_x}{a}\right)^2 + \left(\frac{\tilde{b}^s_y}{b}\right)^2 + \left(\frac{\tilde{b}^s_z}{c}\right)^2}}, \tag{25b}$$

where $b^{MM509}(0.2512\ nm)$, μ^{MM509}, H are the Burgers vector, shear modulus, and Hall-Petch-like barrier effect coefficient, respectively. The shear modulus is obtained using the crystal compliance tensor, $\mathbf{S}(\mathbf{x})$, projected on the slip system using $\frac{1}{\mu_{ijk}} = S_{44} + 4\left(S_{11} - S_{12} - \frac{1}{2}S_{44}\right)\left(l^2_{i1}l^2_{j2} + l^2_{j2}l^2_{k3} + l^2_{i1}l^2_{k3}\right)$ where l_{i1}, l_{j2}, l_{k3} are the direction cosines of the interrogation direction $[ijk]$. The quantities a, b, c are the ellipsoidal dimensions representing a grain and $\hat{b}^s_x$, $\hat{b}^s_y$, $\hat{b}^s_z$ denote the unit vector in Burgers direction in the grain to estimate the dislocation mean-free-path, d^s_{mfp}.

The slip resistance owing to the evolution of statistically stored dislocation density, τ^s_{forest}, is defined using the extended Taylor-type relationship

$$\tau^s_{forest} = b^{MM509}\chi\,\mu^{MM509}\sqrt{\rho^s_{tot} + L^{ss'}\sum_{s\neq s'}\rho^{s'}_{tot}}, \tag{26}$$

whereχdenotes the system interaction parameter taken to be 0.9 (Lavrentev, 1980; Mecking and Kocks, 1981), while $L^{ss'}$ is the latent hardening defined in appendix A. Total stored forest dislocation density, ρ^s_{tot}, is described next.

The total density is divided in two dislocation populations, one being forward and another being reversible (Kitayama et al., 2013), to introduce a deformation path dependence in the hardening law. Furthermore, slip system directions (i.e. s^+, s^-) whether positive or negative on a given plane are assigned to the reversible populations. As a result, the total dislocation density is

$$\rho^s_{tot} = \rho^s_{forw} + \rho^{s+}_{rev} + \rho^{s-}_{rev} \tag{27}$$

with ρ^s_{forw} as the dislocation density correspond to the forward population and ρ^{s+}_{rev}, ρ^{s-}_{rev} as the reversible populations correspond to slip directions $s^+$and s^-.

The forward population is governed by a competition between the rate of storage and the rate of recovery as (Mecking and Kocks, 1981; Zecevic et al., 2016)

$$d\gamma^{s+} > 0 : \frac{\partial\rho^s_{forw}}{\partial\gamma^s} = (1-p)k_1\sqrt{\rho^s_{forw} + \rho^{s+}_{rev}} - k_2(\dot{\varepsilon}, T)\rho^s_{forw}, \tag{28a}$$

$$d\gamma^{s-} > 0 : \frac{\partial\rho^s_{forw}}{\partial\gamma^s} = (1-p)k_1\sqrt{\rho^s_{forw} + \rho^{s-}_{rev}} - k_2(\dot{\varepsilon}, T)\rho^s_{forw}, \tag{28b}$$

where k_1 is a fitting constant driving the rate of generation, while $k_2$drives the rate of recovery (Beyerlein and Tomé, 2008). The constant p is the shear reversibility in the range between 0 and 1 to separate the fraction of forward and reversible populations. For low to moderate strain levels, $p = 1$ (Kitayama et al., 2013) meaning that the dislocations are loosely tangled and all can glide in the opposite direction at the load reversal. The reversible populations depend on the direction of shearing according to

if $d\gamma^{s+} > 0$:

$$\frac{\partial\rho^{s+}_{rev}}{\partial\gamma^s} = pk_1\sqrt{\rho^s_{forw} + \rho^{s+}_{rev}} - k_2(\dot{\varepsilon}, T)\rho^{s+}_{rev}, \tag{29a}$$

$$\frac{\partial\rho^{s-}_{rev}}{\partial\gamma^s} = -k_1\sqrt{\rho^s_{forw} + \rho^{s+}_{rev}}\left(\frac{\rho^{s-}_{rev}}{\rho^s_{tot}}\right)^m, \tag{29b}$$

if $d\gamma^{s-} > 0$:

$$\frac{\partial\rho^{s-}_{rev}}{\partial\gamma^s} = pk_1\sqrt{\rho^s_{forw} + \rho^{s-}_{rev}} - k_2(\dot{\varepsilon}, T)\rho^{s-}_{rev}, \tag{30a}$$

$$\frac{\partial\rho^{s+}_{rev}}{\partial\gamma^s} = -k_1\sqrt{\rho^s_{forw} + \rho^{s-}_{rev}}\left(\frac{\rho^{s+}_{rev}}{\rho^s_{tot}}\right)^m, \tag{30b}$$

with : $\rho^{s+}_{rev}|_{t=0} = \rho^{s-}_{rev}|_{t=0} = 0$, $\rho^s_{forw}|_{t=0} = \rho^s_{initial,}$ where, the power m controls the rate of dislocation recombination and is taken here as 0.5 (Wen et al., 2015). The parameter $k_2(\dot{\varepsilon}, T)$is defined as a function of temperature and strain rate as follows

$$k_2 = \frac{k_1\chi b^{MM509}}{g}\left(1 - \frac{k_B T}{D\left(b^{MM509}\right)^3}\ln\left(\frac{\dot{\varepsilon}}{\dot{\varepsilon}_0}\right)\right), \tag{31}$$

where$g$ is an effective activation enthalpy, k_B is the Boltzmann constant, $\dot{\varepsilon}_0$ is a reference rate of strain set to $10^7\ s^{-1}$, and $D$is the drag stress.

The last term, τ_{deb}, is a consequence of the debris population (Madec et al., 2003) and is defined as

$$\tau_{deb} = 0.086\,\mu^{MM509}b^{MM509}\sqrt{\rho_{deb}}\log\left(\frac{1}{b^{MM509}\sqrt{\rho_{deb}}}\right), \tag{32}$$

where, ρ_{deb} is the debris population, which evolves using

$$d\rho_{deb} = \sum_s qb^{MM509}\sqrt{\rho_{deb}}k_2(\dot{\varepsilon}, T)\rho^s_{tot}|d\gamma^s|, \tag{33}$$

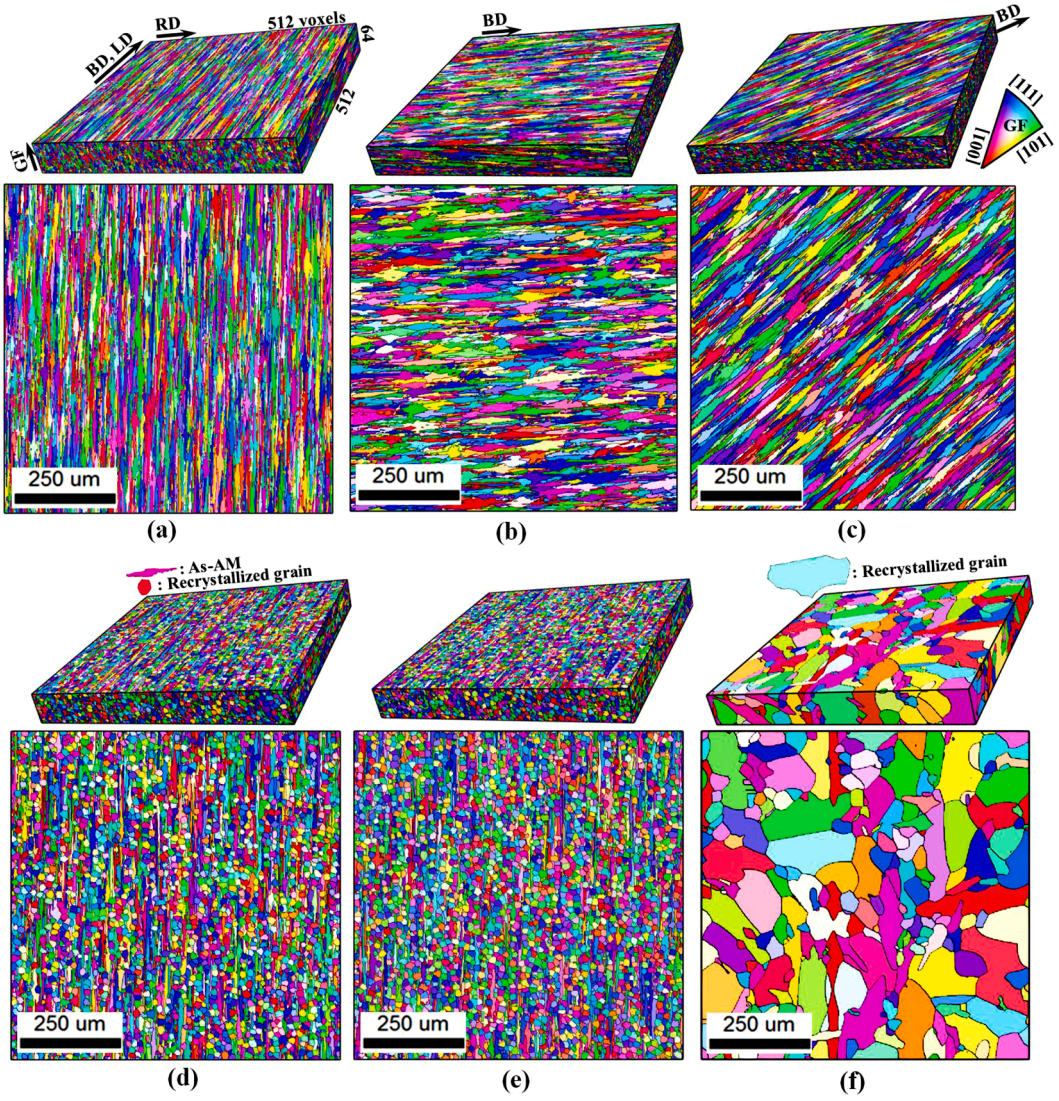

Fig. 1. Microstructural cells for simulations of MM509 Co-based superalloy generated using Dream.3d: (a) as-AM vertical, (b) as-AM Horizontal, (c) as-AM diagonal, (d) 2 h HT (e) 6 h HT and (e) 10 h HT. The first row indicates the 3D RVE microstructures, while the second row shows the 2D projections of their frontal face. In the AM frame, axes are defined as BD for build direction, RD for recoat direction, and GF for gas flow direction (Ferreri et al., 2019). The BD relative to the loading direction (LD) is indicated for all RVEs. The colors in the maps represent the orientation of the gas flow direction axis with respect to the local crystal lattice frame according to the IPF triangle. The recrystallized grains are equiaxed, while non-recrystallized crystals are elongated in the BD. For the 10 h HT material, the equiaxed grains are much larger due to the recrystallization induced grain growth.

where, the parameter q is a fitting parameter to separate the portion of removed dislocations ($\frac{\partial \rho^s_{rem,tot}}{\partial \gamma^s} = k_2(\dot{\varepsilon}, T)\rho^s_{tot,}$) from the debris.

2.3. Back-stress law in MPI-ACC-EVPCUFFT

The evolution of dislocation density and non homogeneous deformation can form geometrically necessary dislocations (GNDs) known to be a source of localized hardening through back-stress fields. Such fields are strain gradients between grains with high contrast in strength (Courtney, 2005). To represent such effects, we adopt a phenomenological approach in which the evolution of back-stress is driven by the plastic strain accommodation in individual crystals. The approach is a computationally efficient simplification of the back-stress estimation in strain gradient plasticity (Lebensohn and Needleman, 2016). Consistent with the self-internal back-stress formulation (Bayley et al., 2006), in our approach only the resolved stress component on a glide plane enters the back-stress definition (Evers et al., 2004; Kim et al., 2012).

The evolution law for the slip system back-stress helping/hindering the deformation of a grain is modeled using the following equations for an increment in shearing $d\gamma^{s+/-} > 0$ (in the forward + / in the reverse – direction) (Eghtesad and Knezevic, 2020; Zecevic and Knezevic, 2018; Zecevic and Knezevic, 2015; Zecevic and Knezevic, 2019; Zecevic and Knezevic, 2017; Zecevic et al., 2017)

$$if \;\; \tau^{s+/-}_{bs,sys} > 0 :$$

$$\overset{*}{\gamma}^{s+/-} = \frac{-1}{\nu}\ln\left(1 - \frac{\tau^{s+/-}_{bs,sys}}{\tau^{sat}_{bs}}\right), \tag{34a}$$

$$\tau^{s+/-}_{bs,sys} = \tau^{sat}_{bs}\left(1 - \exp\left(-\nu\left(\overset{*}{\gamma}^{s+/-} + d\gamma^{s+/-}\right)\right)\right), \tag{34b}$$
$$\tau^{s-/+}_{bs,sys} = -A_{bs}\tau^{s+/-}_{bs,sys},$$

$$elseif \;\; \tau^{s+/-}_{bs,sys} < 0 :$$

Table 1
Microstructural cell parameters for Dream.3D "StatsGenerator" pipelines.

	As-AM Vertical	As-AM Horizontal	As-AM Diagonal	2 h HT	6 h HT	10 h HT
# of grains	9,880	9,939	9,917	18,238	20,927	377
# of voxels	16,777,216	16,777,216	16,777,216	16,777,216	16,777,216	16,777,216
Average # of voxels per grain	1,698	1,688	1,692	920	802	44,502
Equivalent sphere diameter (ESD)	3.33–4.07	3.33–4.07	3.33–4.07	As-AM: 3.33–4.07 Recrystallized: 2.73	As-AM: 3.33–4.07 Recrystallized: 2.73	As-AM: 2.23–6.07 Recrystallized: 20.1862
Feature aspect ratio (a/b, a/c)	4.0104	4.0104	4.0104	2.2472	2.4155	1.7241

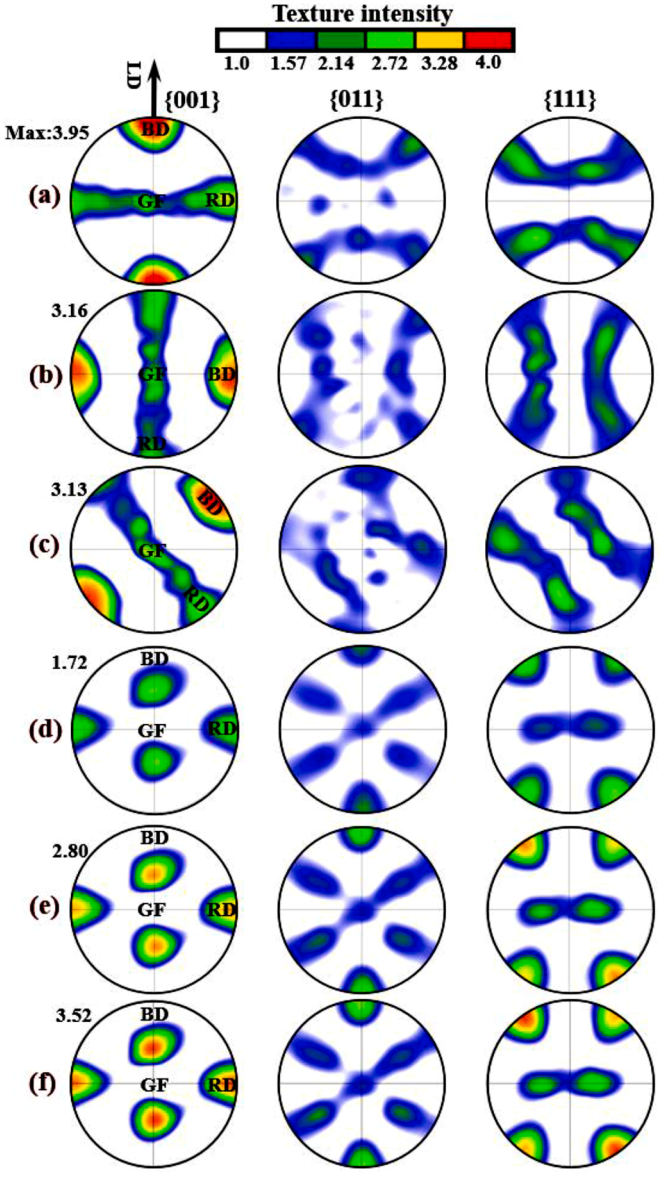

Fig. 2. Experimentally measured (Ferreri et al., 2019) stereographic pole figures showing the textures (i.e., crystallographic orientation distributions) in: (a) AM vertical, (b) AM Horizontal, (c) AM diagonal, (d) 2 h HT vertical and (e) 6 h HT vertical (f) 10 h HT samples of the Co-based MM509 superalloy relative to the loading direction (LD). The texture intensity varies from unity (i.e., uniform distriviution) to 4.0 for all cases.

$$\overset{**}{\gamma}{}^{s+/-} = -\gamma_b \ln\left(\frac{\tau_{bs}^{sat} - \tau_{bs,sys}^{s+/-}}{(A_{bs}+1)\tau_{bs}^{sat}}\right), \tag{34c}$$

$$\tau_{bs,sys}^{s+/-} = -(A_{bs}+1)\tau_{bs,sys}^{s+/-}\exp\left(-\frac{\overset{**}{\gamma}{}^{s+/-} + d\gamma^{s+/-}}{\gamma_b}\right) + \tau_{bs}^{sat}, \tag{34d}$$

$$\tau_{bs,sys}^{s-/+} = -\frac{1}{A_{bs}}\tau_{bs,sys}^{s+/-},$$

where $\tau_{bs,sys}^{s+/-}$ is the back-stress for the two opposite directions, s^+ and s^-. A_{bs} and ν are the back-stress calibration parameters. The parameter A_{bs} can capture any asymmetry in the evolution of the back-stress between two slip directions in the opposite sense, which are responsible for nonlinear unloading at the load reversal (Sritharan and Chandel, 1997). The limit at which the back-stress evolution will saturate τ_{bs}^{sat} is also a calibrating parameter. Note that the grain must deform plastically accommodating some shear of $\gamma^{s+/-}$ in order for the back-stress to evolve.

The slip system back-stress law is defined to capture the local plasticity effects responsible for non-linear unloading and the Bauschinger effect. While $\tau_{bs}^{s^+}$ acts in the direction opposite to the driving stress on s^+, i.e. $\mathbf{P}^{s^+}\cdot\boldsymbol{\sigma} - \tau_{bs}^{s^+} = \tau_c^s$, meaning that $\tau_{bs}^{s^+}$ lowers the driving stress, $\tau_{bs}^{s^-}$ aids the driving stress on the slip system s^- according to: $\mathbf{P}^{s^-}\cdot\boldsymbol{\sigma} - \tau_{bs}^{s^-} = \tau_c^s$.

3. Microstructure, texture, and mechanical response of MM509

Fig. 1 presents the microstructural cells or representative volume elements (RVEs) for samples of as-built AM vertical, as-built AM horizontal, as-built AM diagonal (with 45 rotation relative to the horizontal/vertical microstructures), 2 h HT, 6-h HT, and 10 h HT MM509. The cells visualize the inverse pole figure (IPF) color maps. The resolution is $512 \times 512 \times 64$. Note that the selection of such resolution over a 256^3 which is commonly used in our previously published works is to achieve smooth and as realistic as possible GBs in the RVEs. This is necessary since the heat-treated samples of MM509 show a high contrast of grain shape/size between the elongated grains and equiaxed/round recrystallized grains. As a result, grain boundaries are geometrically complex. Importantly, as the thickness of the RVE slice contains enough number of voxels, we are not limited to plane strain boundary conditions (BCs). In case one or a few voxels are used to discretize the thickness of the slice of RVE, BCs must be adopted to account for plain strain deformations. It is also worth to mention that simulating a $512 \times 512 \times 512$ RVE demands much more GPUs, which were not available at the time of conducting the present research. Table 1 provides the required information input in Dream.3d "StatsGenerator" pipeline to generate the synthetic microstructures attempting to resemble the EBSD measurements as closely as possible. The cells of lower resolution of $128 \times 128 \times 16$ were also created to facilitate simulations with large number of increments. Since these are

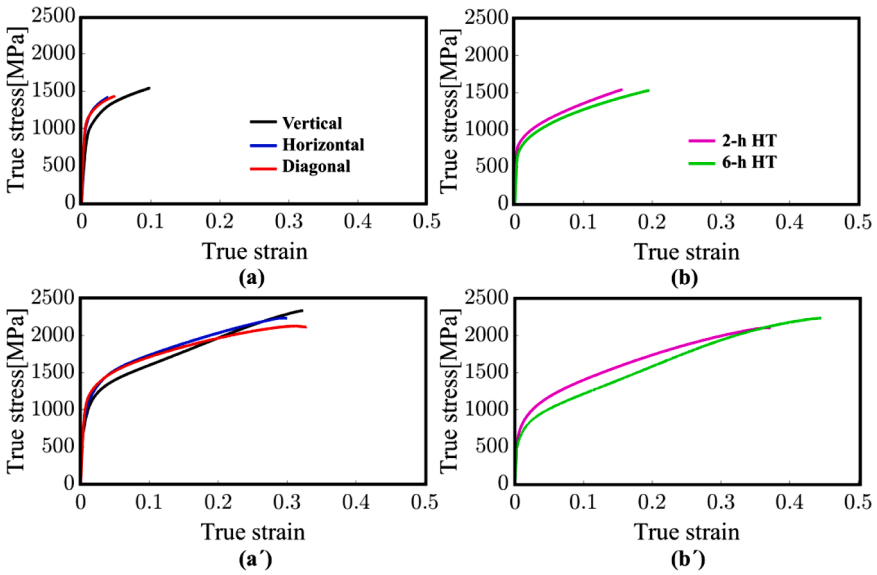

Fig. 3. Experimentally measured (Ferreri et al., 2019) true stress-strain response of alloy MM509 in as-built AM vertical, horizontal, and diagonal directions under (a) tension and (a) compression. Subfigures (b) and (b) illustrate the tension and compression response for 2 h HT and 6 h HT vertical specimens, respectively.

Table 2
Non-Schmid constants.

c_1	c_2	c_3	c_4
0.0	0.0	-0.03	-0.03

Table 3
Single-crystal elastic constants for MM509.

Parameter	Value
C_{11} [MPa]	190,000
C_{12} [MPa]	138,900
C_{44} [MPa]	104,200

visually very similar to the high-resolution cells, they are not shown in the figure. Pole figures showing texture in the microstructures from Fig. 1 are provided in Fig. 2.

Fig. 3 presents measured monotonic compression and tension true stress-true strain curves as a function of build direction and heat treatment (Ferreri et al., 2019). The difference observed in the behavior is owing to the variation in their microstructures. The HT samples experience lower stress owing to the partial or full recrystallization of the structure. Recrystallized grains have lower dislocation density, which is reflected on the strength. Moreover, the strain to which the tensile deformation continues is approximately two times larger for the HT samples compared to the as-built samples.

4. Results and discussion

In order to simulate strength during low-cycle fatigue for the alloy, we begin by modeling the monotonic response in tension and compression and then the load reversals. The hardening law parameters are fit to reproduce the monotonic data. Subsequently, the back-stress law parameters are calibrated to reproduce the large strain cyclic data. Finally, the model is adjusted to simulate the LCF data. Results pertaining to these calculations are presented and discussed in this section.

4.1. Modeling of tension/compression monotonic response

The monotonic deformation behavior of MM509 is simulated using

Table 4
Effective grain shape per material.

	As-AM Vertical	As-AM Horizontal	As-AM Diagonal	2 h HT	6 h HT	10 h HT
$a\,[\mu m]$	73.51	18.33	45.92	43.89	47.39	137.91
$b\,[\mu m]$	18.33	73.51	45.92	19.52	19.64	79.96
$c\,[\mu m]$	18.33	18.33	18.33	19.52	19.64	79.96

the non-Schmid parameters, elastic constants, grain shape, and hardening law parameters provided in Tables 2–5, respectively. The calibration of these constants is performed simultaneously by slightly varying the volume fraction of recrystallized grains in the heat treatments samples until a good fit is obtained. Recrystallized grains had the initial dislocation density lower than the as-built grains (Table 5). Recrystallized grains are approximately strain free, generally equiaxed, and have low dislocation density. In contrast, as-built acicular grains have higher microstrain and greater dislocation content as a consequence of rapid heating/cooling during AM. The initial estimating of the % recrystallization was based on the grains aspect ratio (GAR) contours obtained from experiments presented in (Ferreri et al., 2019). This required to re-run the Dream.3d to generate microstructures with the recrystallized phase of varying volume fraction. The discrete microstructures in a given range of the phases are simulated and those which yielded the best agreement with experimental data estimated % recrystallization. The calibration against experimental data are depicted in Fig. 4. The inferred volume fractions by the fitting process are

Table 5
Hardening parameters.

Parameter	Value
$\tau_0\,[MPa]$	40
$k_1\,[m^{-1}]$	6.0e8
$D\,[MPa]$	80.0
g	0.65
$\rho_{0,forest,\ as-AM}\,[m^{-2}]$	5.0e14
$\rho_{0,forest,\ recrystallized}\,[m^{-2}]$	1.0e12
H	0.8
q	0.1
$\mu^{MARM509}\,[GPa]$	41.04

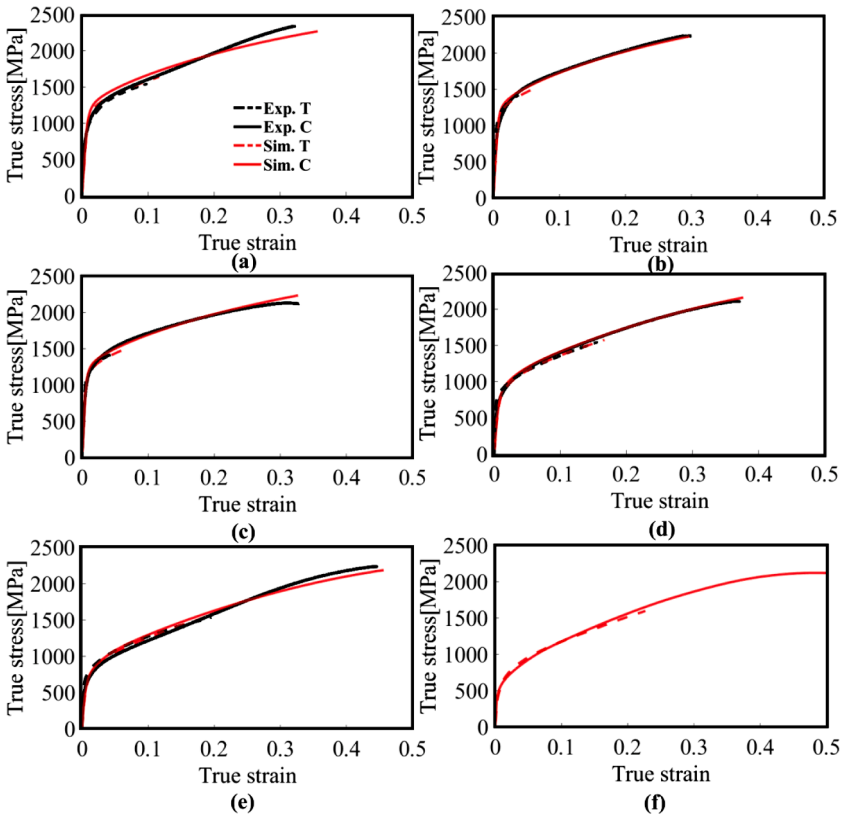

Fig. 4. Measured (Exp.) and simulated (Sim.) monotonic loading response in tension (shorter curves) and compression (curves to large strains > 0.3) for samples of MM509: (a) as-AM vertical, (b) as-AM Horizontal, (c) as-AM diagonal, (d) 2 h HT, (e) 6 h HT, and (f) predicted 10 h HT.

Table 6
Latent hardening parameters (Ghorbanpour et al., 2017, Hoc et al., 2004, Devincre et al., 2006).

a_0	a_1	a_2	a_3	a_4	a_5
0.068	0.068	0.0454	0.625	0.137	0.122

Table 7
% recrystallization found for heat treated samples from data calibration.

% Recrystallization	2 h HT	6 h HT	10 h HT
	46	57	91

presented in Table 7. It is important to note that a single set of parameters are used to fit the stress-strain response of the deformation of all the samples of MM509. As is evident, the model successfully predicts anisotropy, which is primarily governed by the dislocation mean-free-path, which changes with respect to the loading axis in a

Table 8
Back-stress fitting parameters.

Parameter	Value
ν	500
A_{bs}	4.9
γ_b	0.01
$\tau_{bs}^{sat}[MPa]$	75.0

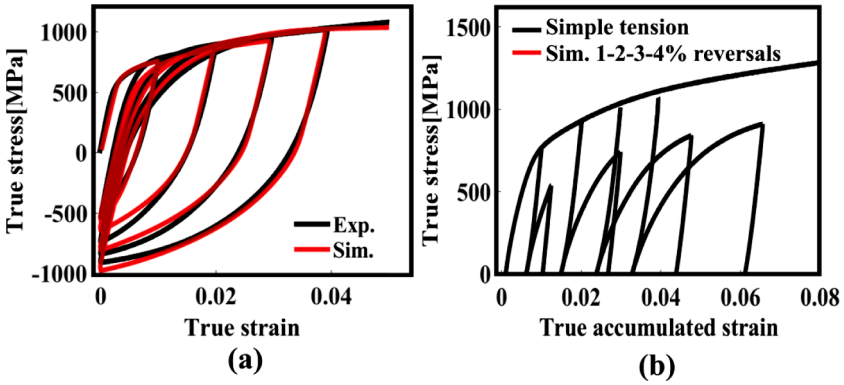

Fig. 5. (a) Comparison of measured (Exp.) and fitted (Sim.) true stress-true strain response of MM509 samples built in the vertical direction under multiple large strain tension-compression cycles pre-strained in tension to 0.01, 0.02, 0.03, and 0.04. (b) Forward and the 1–4 reversal curves as a function of accumulated true strain showing drops in yield stress in compression.

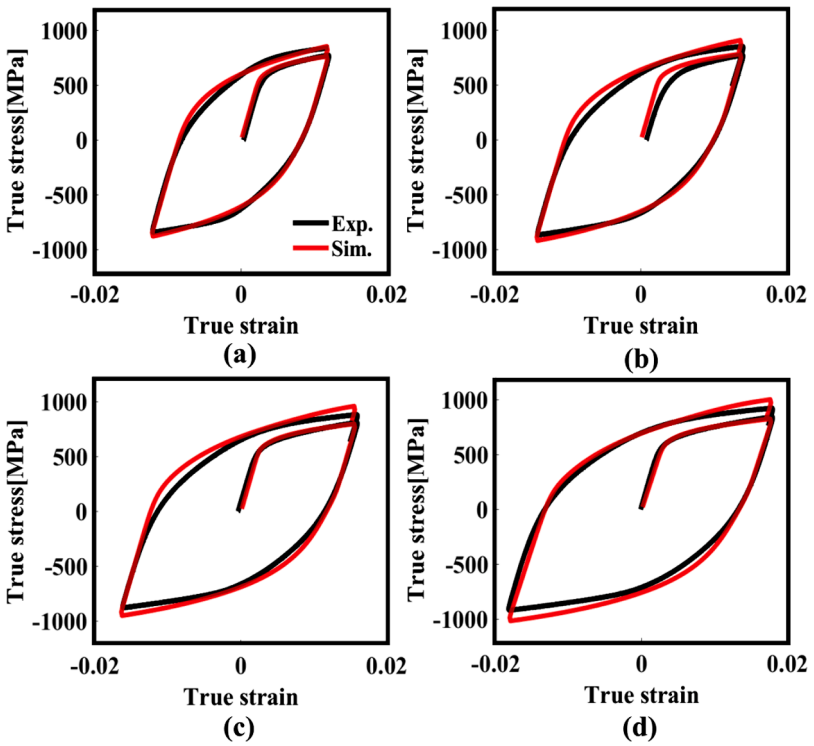

Fig. 6. Comparison of measured (Exp.) and predicted (Sim.) response in the first LCF cycle for as-AM MM509 vertical samples as a function of applied strain: (a) 1.2%, (b) 1.4% (c) 1.6%, and (d) 1.8%.

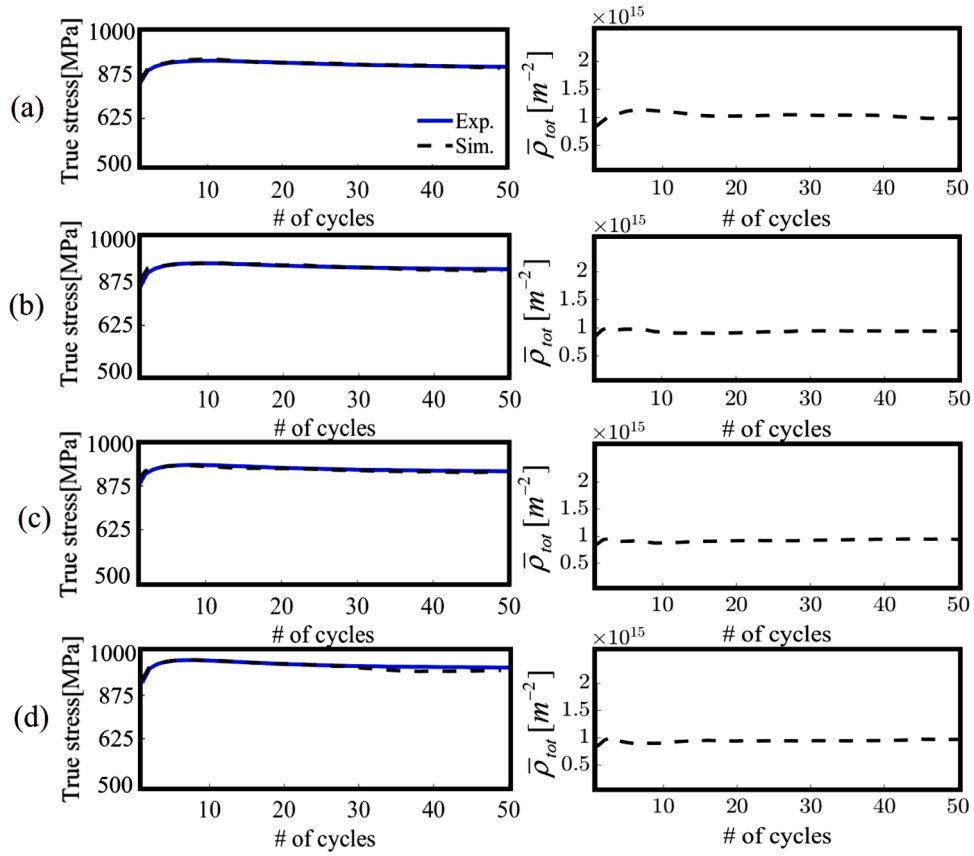

Fig 7. Evolution of stress-amplitudes and total dislocation density with cycles for as-AM vertical samples of MM509 at strain amplitudes of: (a) 1.2%, (b) 1.4%, (c) 1.6%, and (d) 1.8%.

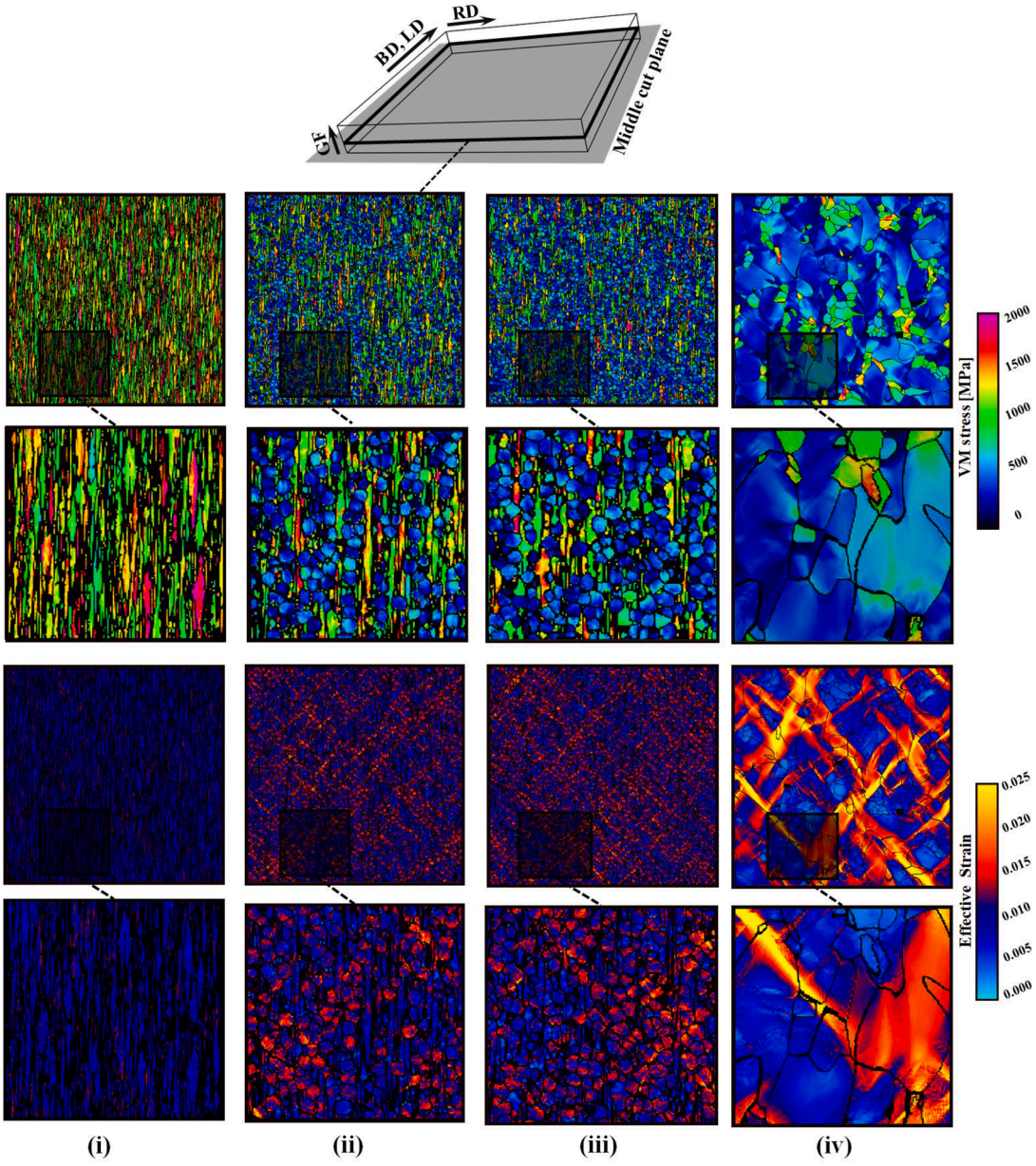

Fig. 8. Contours of von Mises (VM) stress and effective strain after simple tension to a total effective macroscopic strain of 1% over the microstructural cells of MM509 for (i) as-AM vertical (ii) 2 h HT (iii) 6 h HT and (iv) 10 h HT.

microstructure i.e. effective grain shape (Table 4). The non-Schmid effects give rise to the small asymmetry in the response. The decrease in strength with HT is obtained by % recrystallized grains. While the experimental data for the 10 h HT sample was not available, the simulation predictions are included for completeness of the results.

4.2. Modeling of large strain reversal response

In order to calibrate the model for cyclic loadings, a 1–4% cyclic deformation data pertaining to AM vertical sample is utilized and the back-stress parameters are adjusted such that the hysteresis loops are fit against the experimental data (Fig. 5). The back-stress parameters provided in Table 8 were established while calibrating the model to reproduce the cyclic response of the alloy. As is evident, the model successfully reproduces phenomena pertaining to the load reversal deformation such as nonlinear unloading and the Bauschinger effect.

4.3. Modeling strength during LCF

Fig. 6 depicts a comparison between measured and simulated first cycles of LCF under strain amplitudes of 1.2, 1.4, 1.6, and 1.8% for as-AM vertical MM509 samples at room temperature. These simulations results are predictions. While the initial LCF deformation usually increase DD, subsequent LCF deformation is governed by a combination of dislocation generation and annihilation (Zong and Wu, 2017). As a result, cyclic softening occurs. Fig. 7 shows the calibration of the model for 50 cycles of LCF to reproduce the evolution of stress amplitude. The evolution of stress amplitude plateaus after 50 cycles. In doing so, the total dislocation density evolution is extracted per grain and per slip system. The sum over the slip systems averaged over the grains is plotted with cycles per simulation in Fig. 7. The fitting process demands a lot of trial and error which is relatively computationally expensive despite running the simulations on the GPU hardware. Results indicate that the annihilation mechanism utilized in the model can successfully capture the deformation softening behavior of the alloy under LCF loading. In

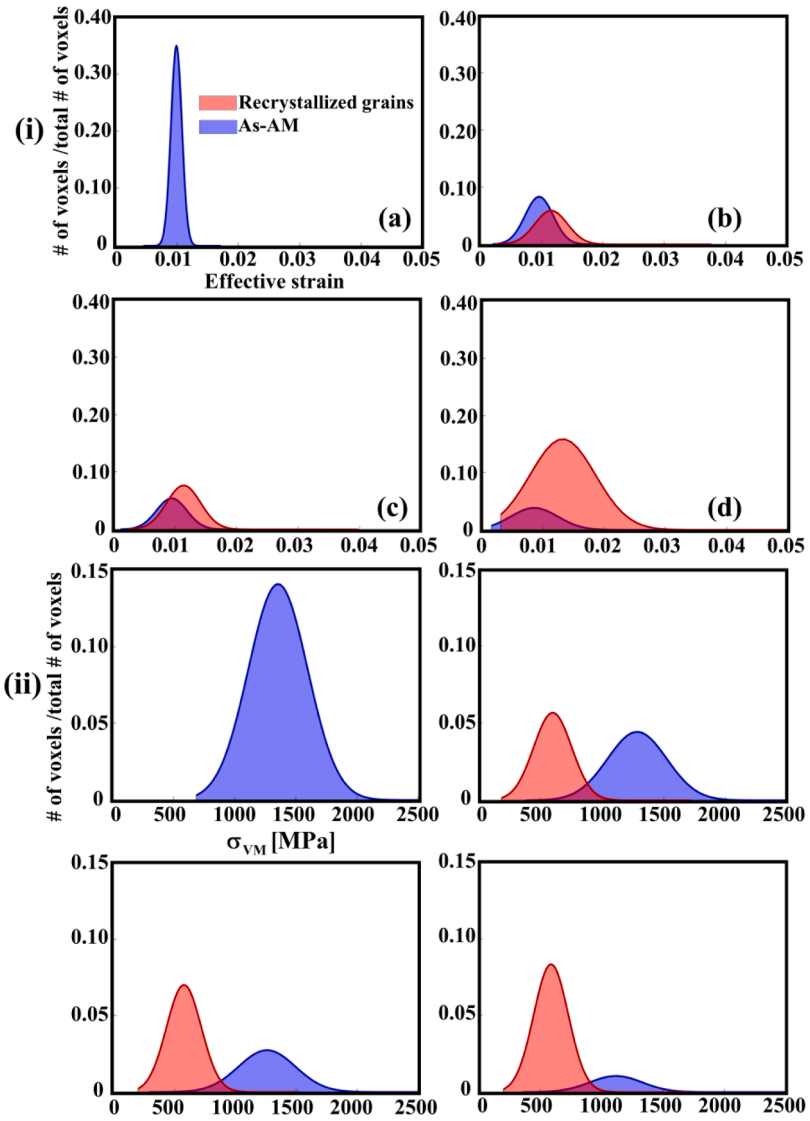

Fig. 9. Distribution of effective strain (i) and VM stress (ii) within RVEs of MM509 for recrystallized and non- recrystallized grains after simple tension to an effective macroscopic strain of 1% for (a) as-AM vertical, (b) 2 h HT, (c) 6 h HT, and (d) 10 h HT samples.

summary, anisotropy, tension/compression asymmetry, unloading, Bauschinger effect, and cyclic hardening/softening can be successfully reproduced by the model adapted for the alloy. Moreover, evolution of dislocation density during LCF can be inferred while predicting the evolution of strength during LCF using the model.

4.4. Micromechanical strain-stress fields as revealed by the model

Calibration of macroscopic response of the MM509 alloy is followed by examining the distribution of micromechanical fields over the microstructural cells. The AM vertical and the three heat treated samples are subjected to simple tension deformation up to 1% strain and the resulted effective strain and von Mises (VM) stress fields are depicted in Fig. 8. The model predicts that larger strains are accommodated by the recrystallized grains of the heat-treated specimens. From (i) to (iv) we observe higher levels of strain within softer recrystallized grains in the material, which would lead to the increase in ductility. Interestingly, strain and stress within the grains do not always follow the expected trends (grains with higher strain experiencing lower stress or vice versa). The strain contours follow the 45° orientation relative to the LD. Finally, Fig. 9(i) and (ii) illustrate the distribution of the strain and VM stress magnitudes for as-AM and recrystallized grains. The stress-strain partitioning between strains can be observed for each simulation.

5. Performance benchmarks

The computational efficiency of the solver is illustrated using a performance benchmark on 8 NVIDIA Tesla V100 GPUs (32 GB) installed on the high-performance cluster at the University of New Hampshire (NH BioMade supercomputer). The utilization is facilitated by MPI+OpenACC parallelization developed earlier in (Eghtesad et al., 2020). The hardware specification of the cluster is provided in Table 9. The benchmarks are obtained for monotonic, LCF, and high-resolution full-field simulations. Table 10 shows the computational time involved for the performed simulation benchmarks. Utilizing multiple GPUs enables us to perform the most computationally intensive simulations of full-field crystal plasticity in orders of few hours instead of month of run times. This is indeed a promising development towards a unique high-performance crystal plasticity computational platform which utilizes high-end GPUs of supercomputers to perform precise and efficient modelling, analysis, and design of mechanical components and assemblies for real-world applications in various industries.

Table 9
Hardware specs of the NH BioMade supercomputer.

Cluster	# of utilized nodes	Compiler	OS	CPU	GPU per node	# of GPUs per node	CUDA toolkit version	System memory (GB)	# of CPUs	# of threads per core	# of sockets	# of cores per socket
NH BioMade	8	PGI v 2019 v19.7	Centos 7.6	Intel(R) Xeon(R) Gold 6130 CPU @ 2.10GHz	NVIDIA Tesla V100 (32 GB)	1	10.1	800	32	2	2	16

Table 10
Simulation benchmarks on NH BioMade supercomputer running parallel on 8 distributed NVIDIA Tesla V100 GPUs.

Deformation type	Strain	RVE resolution	Wall clock time (h)
Monotonic compression (AM Vertical)	0.323 (true strain)	$128 \times 128 \times 16$	0.1301
Monotonic tension (AM Vertical)	0.098 (true strain)	$128 \times 128 \times 16$	0.0423
LCF (AM Vertical)	50 cycles, 1.8% strain amplitude	$128 \times 128 \times 16$	2.2616
High resolution fields (AM Vertical)	0.02 (true strain)	$512 \times 512 \times 64$	4.8309
High resolution fields (2 h HT)	0.02 (true strain)	$512 \times 512 \times 64$	4.8171
High resolution fields (6 h HT)	0.02 (true strain)	$512 \times 512 \times 64$	4.8722
High resolution fields (10 h HT)	0.02 (true strain)	$512 \times 512 \times 64$	4.7389

6. Summary and conclusions

The effective and micromechanical properties of additively manufactured Co-based alloy MM509 are simulated utilizing a GPU accelerated full-field spectral crystal plasticity model. To initialize the model setups for simulating mechanical properties of the alloy in different conditions, voxel-based microstructural cells are created for as-AM vertical, horizontal, and diagonal specimens and for 2, 6, and 10 h heat treated vertical specimens synthetically using Dream.3d. Measured microstructure features including grain size/shape, texture, and % recrystallized material are embedded in the cells to resemble the experimental EBSD maps/data. The variation in such microstructural features in the samples as a consequence of their processing history facilitated accurate calibration of the model using monotonic compression and tension data. In addition to calibrating the hardening parameters along with the initial dislocation density of the as-built versus recrystallized grains, % recrystallized is adjusted to reproduce the strength of the heat treated materials. Furthermore, the load reversal data facilitated accurate calibration of the model's back-stress kinematic hardening law to capture the cyclic hysteresis loops. Notably, a single set of model parameters is established for the alloy to predict properties for a range of microstructures under a variety of loadings. Tension/compression yield asymmetry, anisotropy, nonlinear unloading, the Bauschinger effect, and hardening rates are simultaneously predicted. By comparing the model predictions and the measured data, it is found that the initial grain morphology governs anisotropy of the material, while the tension/compression asymmetry is promoted by the modified relation for the activation of slip systems. The secondary effects come from texture and the latent hardening. The decrease in strength with HT is obtained by % recrystallized grains. Moreover, the model is calibrated to predict the evolution of strength i.e. the cyclic hardening/softening observed in the LCF experiments. In doing so, the evolution of dislocation density during LCF is inferred. Finally, the micromechanical strain and stress fields are quantified over the microstructures providing insights into the partitioning of stress and accommodated strain by the as-AM and recrystallized grains. In general, soft grains accommodate more strain, while hard grains promote higher stress. However, the local effects significantly influence such trends. Future work will attempt to further enhance the present model to consider a damage/failure criteria given that the critical mechanical fields to assess the effect of deformation on the localizations in the microstructure can be predicted by the present model. In addition to the predictive characteristics, the key advantage of the MPI-ACC-EVPCUFFT model is in its computational efficiency and versatility to be adapted for other metals.

Declaration of Competing Interest

The authors declare that they have no known competing financial interests or personal relationships that could have appeared to influence the work reported in this paper.

Acknowledgments

This research is sponsored by the U.S. National Science Foundation and accomplished under the CAREER Grant No. CMMI-1650641. A. E. also acknowledges support from the Dissertation Year Fellowship (DYF) program at the University of New Hampshire.

Appendix A

The generalized interaction matrix representing latent hardening for FCC metals is presented below. $A_2, A_3, A_6, B_2, B_4, B_5, C_1, C_3, C_5, D_1, D_4$ and D_6 are the slip systems, where A–D represent the $(\bar{1}11), (111), (\bar{1}\bar{1}1)$ and $(1\bar{1}1)$ slip planes, while the numbers 1–6 denote the $[011], [0\bar{1}1], [101], [\bar{1}01], [\bar{1}10]$ and $[110]$ slip directions. The constants $a_0, a_1, a_2, a_3, a_4, a_5$ for MM509 are given in Table 6.

	A_2	A_3	A_3	B_2	B_4	B_5	C_1	C_3	C_5	D_1	D_4	D_6
A_2	a_0	a_1	a_1	a_3	a_4	a_4	a_2	a_4	a_5	a_2	a_5	a_4
A_3		a_0	a_1	a_4	a_2	a_5	a_4	a_3	a_4	a_5	a_2	a_4
A_6			a_0	a_4	a_5	a_2	a_5	a_4	a_2	a_4	a_4	a_3
B_2				a_0	a_1	a_1	a_2	a_5	a_4	a_2	a_4	a_5
B_4					a_0	a_1	a_5	a_2	a_4	a_4	a_3	a_4
B_5						a_0	a_4	a_4	a_3	a_5	a_4	a_2
C_1							a_0	a_1	a_1	a_3	a_4	a_4
C_3								a_0	a_1	a_4	a_2	a_5
C_5									a_0	a_4	a_5	a_2
D_1										a_0	a_1	a_1
D_4											a_0	a_1
D_6												a_0

References

Akande, I.G., Oluwole, O.O., Fayomi, O.S.I, Odunlami, O.A., 2021. Overview of mechanical, microstructural, oxidation properties and high-temperature applications of superalloys. Mater. Today Proc. 43, 2222–2231. https://doi.org/10.1016/j.matpr.2020.12.523.

Ardeljan, M., Knezevic, M., 2018. Explicit modeling of double twinning in AZ31 using crystal plasticity finite elements for predicting the mechanical fields for twin variant selection and fracture analyzes. Acta Mater. 157, 339–354.

Ardeljan, M., Beyerlein, I.J., Knezevic, M., 2014. A dislocation density based crystal plasticity finite element model: application to a two-phase polycrystalline HCP/BCC composites. J. Mech. Phys. Solids 66, 16–31.

Ardeljan, M., McCabe, R.J., Beyerlein, I.J., Knezevic, M., 2015. Explicit incorporation of deformation twins into crystal plasticity finite element models. Comput. Meth. Appl. Mech. Eng. 295, 396–413.

Ardeljan, M., Beyerlein, I.J., McWilliams, B.A., Knezevic, M., 2016. Strain rate and temperature sensitive multi-level crystal plasticity model for large plastic deformation behavior: Application to AZ31 magnesium alloy. Int. J. Plast. 83, 90–109.

Ardeljan, M., Savage, D.J., Kumar, A., Beyerlein, I.J., Knezevic, M., 2016. The plasticity of highly oriented nano-layered Zr/Nb composites. Acta Mater. 115, 189–203.

Ardeljan, M., Beyerlein, I.J., Knezevic, M., 2017. Effect of dislocation density-twin interactions on twin growth in AZ31 as revealed by explicit crystal plasticity finite element modeling. Int. J. Plast. 99, 81–101.

Asaro, R.J., Needleman, A., 1985. Texture development and strain hardening in rate dependent polycrystals. Acta Metall. Mater. 33, 923–953.

Barrett, T.J., Knezevic, M., 2019. Deep drawing simulations using the finite element method embedding a multi-level crystal plasticity constitutive law: experimental verification and sensitivity analysis. Comput. Meth. Appl. Mech. Eng. 354, 245–270.

Barrett, T.J., Savage, D.J., Ardeljan, M., Knezevic, M., 2018. An automated procedure for geometry creation and finite element mesh generation: Application to explicit grain structure models and machining distortion. Comput. Mater. Sci. 141, 269–281.

Barrett, T.J., Eghtesad, A., McCabe, R.J., Clausen, B., Brown, D.W., Vogel, S.C., Knezevic, M., 2019. A generalized spherical harmonics-based procedure for the interpolation of partial datasets of orientation distributions to enable crystal mechanics-based simulations. Materialia 6, 100328.

Barrett, T.J., McCabe, R.J., Brown, D.W., Clausen, B., Vogel, S.C., Knezevic, M., 2020. Predicting deformation behavior of α-uranium during tension, compression, load reversal, rolling, and sheet forming using elasto-plastic, multi-level crystal plasticity coupled with finite elements. J. Mech. Phys. Solids 138, 103924.

Bayley, C.J., Brekelmans, W.A.M., Geers, M.G.D., 2006. A comparison of dislocation induced back stress formulations in strain gradient crystal plasticity. Int. J. Solids Struct. 43, 7268–7286.

Beaudoin, A.J., Dawson, P.R., Mathur, K.K., Kocks, U.F., Korzekwa, D.A., 1994. Application of polycrystal plasticity to sheet forming. Comput. Methods Appl. Mech. Eng. 117, 49–70.

Bellman, R., Adomian, G., 1985. Green's functions for partial differential equations. Partial Differential Equations. Springer, pp. 243–247.

Beyerlein, I.J., Tomé, C.N., 2008. A dislocation-based constitutive law for pure Zr including temperature effects. Int. J. Plast. 24, 867–895.

Bišs, V., 1977. Phase analysis of standard and molybdenum-modified Mar-M509 superalloys. J. Test. Eval. 5, 217–223.

Biss, V., 1977. Phase analysis of standard and molybdenum-modified Mar-M509 superalloys. J. Test. Eval. 5, 217–223.

Bronkhorst, C.A., Mayeur, J.R., Livescu, V., Pokharel, R., Brown, D.W., Gray, G.T., 2019. Structural representation of additively manufactured 316L austenitic stainless steel. Int. J. Plast.

Cantara, A.M., Zecevic, M., Eghtesad, A., Poulin, C.M., Knezevic, M., 2019. Predicting elastic anisotropy of dual-phase steels based on crystal mechanics and microstructure. Int. J. Mech. Sci. 151, 639–649.

Chen, Z., Phan, M., Darvish, K., 2017. Grain growth during selective laser melting of a Co-Cr-Mo alloy. J. Mater. Sci. 52, 7415–7424.

Cloots, M., Kunze, K., Uggowitzer, P., Wegener, K., 2016. Microstructural characteristics of the nickel-based alloy IN738LC and the cobalt-based alloy Mar-M509 produced by selective laser melting. Mater. Sci. Eng. A 658, 68–76.

Courtney, T.H., 2005. Mechanical Behavior of Materials. Waveland Press.

Cruzado, A., LLorca, J., Segurado, J., 2017. Modeling cyclic deformation of inconel 718 superalloy by means of crystal plasticity and computational homogenization. Int. J. Solids Struct. 122, 148–161.

Cruzado, A., Lucarini, S., LLorca, J., Segurado, J., 2018. Crystal plasticity simulation of the effect of grain size on the fatigue behavior of polycrystalline Inconel 718. Int. J. Fatigue 113, 236–245.

Davis, J.R., ASM International, 1997. Handbook Committee, Heat-Resistant Materials. ASM International, Materials Park, Ohio.

Devincre, B., Kubin, L., Hoc, T., 2006. Physical analyzes of crystal plasticity by DD simulations. Scr. Mater. 54, 741–746.

Ding, R., Knaggs, C., Li, H., Li, Y.G., Bowen, P., 2020. Characterization of plastic deformation induced by machining in a Ni-based superalloy. Mater. Sci. Eng. A 778, 139104.

Drapier, J.M.L., Dupont, C., Coutsouradis, D., Habraken, L., 1968. Structural Stability of Mar-M-509 - A Cobalt-Base Superalloy. TMS, pp. 436–459.

Eghtesad, A., Knezevic, M., 2020. High-performance full-field crystal plasticity with dislocation-based hardening and slip system back-stress laws: application to modeling deformation of dual-phase steels. J. Mech. Phys. Solids 134, 103750.

Eghtesad, A., Zecevic, M., Lebensohn, R.A., McCabe, R.J., Knezevic, M., 2018. Spectral database constitutive representation within a spectral micromechanical solver for computationally efficient polycrystal plasticity modelling. Comput. Mech. 61, 89–104.

Eghtesad, A., Barrett, T.J., Germaschewski, K., Lebensohn, R.A., McCabe, R.J., Knezevic, M., 2018. OpenMP and MPI implementations of an elasto-viscoplastic fast Fourier transform-based micromechanical solver for fast crystal plasticity modeling. Adv. Eng. Softw. 126, 46–60.

Eghtesad, A., Barrett, T.J., Knezevic, M., 2018. Compact reconstruction of orientation distributions using generalized spherical harmonics to advance large-scale crystal plasticity modeling: verification using cubic, hexagonal, and orthorhombic polycrystals. Acta Mater. 155, 418–432.
Eghtesad, A., Germaschewski, K., Beyerlein, I.J., Hunter, A., Knezevic, M., 2018. Graphics processing unit accelerated phase field dislocation dynamics: application to bi-metallic interfaces. Adv. Eng. Softw. 115, 248–267.
Eghtesad, A., Germaschewski, K., Lebensohn, R.A., Knezevic, M., 2020. A multi-GPU implementation of a full-field crystal plasticity solver for efficient modeling of high-resolution microstructures. Comput. Phys. Commun., 107231
Evers, L.P., Brekelmans, W.A.M., Geers, M.G.D., 2004. Non-local crystal plasticity model with intrinsic SSD and GND effects. J. Mech. Phys. Solids 52, 2379–2401.
Feather, W.G., Ghorbanpour, S., Savage, D.J., Ardeljan, M., Jahedi, M., McWilliams, B.A., Gupta, N., Xiang, C., Vogel, S.C., Knezevic, M., 2019. Mechanical response, twinning, and texture evolution of WE43 magnesium-rare earth alloy as a function of strain rate: experiments and multi-level crystal plasticity modeling. Int. J. Plast. 120, 180–204.
Feather, W.G., Lim, H., Knezevic, M., 2020. A numerical study into element type and mesh resolution for crystal plasticity finite element modeling of explicit grain structures. Comput. Mech.
Feather, W.G., Savage, D.J., Knezevic, M., 2021. A crystal plasticity finite element model embedding strain-rate sensitivities inherent to deformation mechanisms: application to alloy AZ31. Int. J. Plast. 143, 103031.
Feng, K.Y., Liu, P., Li, H.X., Sun, S.Y., Xu, S.B., Li, J.N., 2017. Microstructure and phase transformation on the surface of Inconel 718 alloys fabricated by SLM under 1050°C solid solution+ double ageing. Vacuum 145, 112–115.
Ferreri, N.C., Ghorbanpour, S., Bhowmik, S., Lussier, R., Bicknell, J., Patterson, B.M., Knezevic, M., 2019. Effects of build orientation and heat treatment on the evolution of microstructure and mechanical properties of alloy Mar-M-509 fabricated via laser powder bed fusion. Int. J. Plast. 121, 116–133.
Ferreri, N.C., Vogel, S.C., Knezevic, M., 2020. Determining volume fractions of γ, γ′, γ″, δ, and MC-carbide phases in Inconel 718 as a function of its processing history using an advanced neutron diffraction procedure. Mater. Sci. Eng. A 781, 139228.
Ferreri, N.C., Savage, D.J., Knezevic, M., 2020. Non-acid, alcohol-based electropolishing enables high-quality electron backscatter diffraction characterization of titanium and its alloys: application to pure Ti and Ti-6Al-4V. Mater. Charact. 166, 110406.
Ferreri, N.C., Pokharel, R., Livescu, V., Brown, D.W., Knezevic, M., Park, J.S., Torrez, M. A., Gray, G.T., 2020. Effects of heat treatment and build orientation on the evolution of ϵ and α′ martensite and strength during compressive loading of additively manufactured 304L stainless steel. Acta Mater. 195, 59–70.
Frazier, W.E., 2014. Metal additive manufacturing: a review. J. Mater. Eng. Perform. 23, 1917–1928.
Fuentes-Cobas, L.E., Muñoz-Romero, A., Montero-Cabrera, M.E., Fuentes-Montero, L., Fuentes-Montero, M.E., 2013. Predicting the coupling properties of axially-textured materials. Materials 6, 4967–4984.
Galiullin, T., Gobereit, B., Naumenko, D., Buck, R., Amsbeck, L., Neises-von Puttkamer, M., Quadakkers, W., 2019. High temperature oxidation and erosion of candidate materials for particle receivers of concentrated solar power tower systems. Sol. Energy 188, 883–889.
Ghorbanpour, S., Zecevic, M., Kumar, A., Jahedi, M., Bicknell, J., Jorgensen, L., Beyerlein, I.J., Knezevic, M., 2017. A crystal plasticity model incorporating the effects of precipitates in superalloys: application to tensile, compressive, and cyclic deformation of Inconel 718. Int. J. Plast. 99, 162–185.
Ghorbanpour, S., Zecevic, M., Kumar, A., Jahedi, M., Bicknell, J., Jorgensen, L., Beyerlein, I.J., Knezevic, M., 2017. A crystal plasticity model incorporating the effects of precipitates in superalloys: application to tensile, compressive, and cyclic deformation of Inconel 718. Int. J. Plasticity 99, 162–185.
Gong, X., Manogharan, G., 2020. Machining behavior and material properties in additive manufacturing Ti-6Al-4V Parts. In: Proceedings of the 15th International Manufacturing Science and Engineering Conference. American Society of Mechanical Engineers. V001T001A055.
Gribbin, S., Ghorbanpour, S., Ferreri, N.C., Bicknell, J., Tsukrov, I., Knezevic, M., 2019. Role of grain structure, grain boundaries, crystallographic texture, precipitates, and porosity on fatigue behavior of Inconel 718 at room and elevated temperatures. Mater. Charact. 149, 184–197.
Groeber, M.A., Jackson, M.A., 2014. DREAM. 3D: a digital representation environment for the analysis of microstructure in 3D. Integr. Mater. Manuf, Innov. 3, 5.
Herderick, E., 2015. Progress in additive manufacturing. JOM 67, 580–581.
Hoc, T., Devincre, B., Kubin, L., 2004. Deformation stage I of FCC crystals: constitutive modeling. In: Proceedings of the 25th Riso International Symposium on Materials Science, pp. 43–59.
Huang, L., Cao, Y., Li, G., Wang, Y., 2020. Microstructure characteristics and mechanical behavior of a selective laser melted Inconel 718 alloy. J. Mater. Res. Technol. 9, 2440–2454.
Hutchinson, J.W., 1976. Bounds and self-consistent estimates for creep of polycrystalline materials. Proc. R. Soc. Lond. Ser. A Math. Phys. Sci. 348, 101–126.
Kalidindi, S.R., Bronkhorst, C.A., Anand, L., 1992. Crystallographic texture evolution in bulk deformation processing of FCC metals. J. Mech. Phys. Solids 40, 537–569.
Kalidindi, S.R., Duvvuru, H.K., Knezevic, M., 2006. Spectral calibration of crystal plasticity models. Acta Mater. 54, 1795–1804.
Kaschel, F., Celikin, M., Dowling, D.P., 2020. Effects of laser power on geometry, microstructure and mechanical properties of printed Ti-6Al-4V parts. J. Mater. Process. Technol. 278, 116539.
Kergaßner, A., Mergheim, J., Steinmann, P., 2018. Single crystal plasticity–A mesoscale based approach for modeling the mechanics of additively manufactured Inconel 718. PAMM 18, e201800389.
Kim, J.H., Kim, D., Barlat, F., Lee, M.G., 2012. Crystal plasticity approach for predicting the Bauschinger effect in dual-phase steels. Mater. Sci. Engi. A 539, 259–270.
Kitayama, K., Tomé, C., Rauch, E., Gracio, J., Barlat, F., 2013. A crystallographic dislocation model for describing hardening of polycrystals during strain path changes. Application to low carbon steels. Int. J. Plast. 46, 54–69.
Knezevic, M., Ghorbanpour, S., 2018. Modeling Tensile, Compressive, and Cyclic Response of Inconel 718 Using a Crystal Plasticity Model Incorporating the Effects of Precipitates. Springer International Publishing, Cham, pp. 655–668.
Knezevic, M., Kalidindi, S.R., 2007. Fast computation of first-order elastic-plastic closures for polycrystalline cubic-orthorhombic microstructures. Comput. Mater. Sci. 39, 643–648.
Knezevic, M., Kalidindi, S.R., 2017. Crystal plasticity modeling of microstructure evolution and mechanical fields during processing of metals using spectral databases. JOM 69, 830–838.
Knezevic, M., Savage, D.J., 2014. A high-performance computational framework for fast crystal plasticity simulations. Comput. Mater. Sci. 83, 101–106.
Knezevic, M., Kalidindi, S.R., Fullwood, D., 2008. Computationally efficient database and spectral interpolation for fully plastic Taylor-type crystal plasticity calculations of face-centered cubic polycrystals. Int. J. Plasticity 24, 1264–1276.
Knezevic, M., Al-Harbi, H.F., Kalidindi, S.R., 2009. Crystal plasticity simulations using discrete Fourier transforms. Acta Mater. 57, 1777–1784.
Knezevic, M., Levinson, A., Harris, R., Mishra, R.K., Doherty, R.D., Kalidindi, S.R., 2010. Deformation twinning in AZ31: influence on strain hardening and texture evolution. Acta Mater. 58, 6230–6242.
Knezevic, M., Chun, B.K., Oh, J.Y., Wu, W.T., Ress Iii, R.A., Glavicic, M.G., Srivatsa, S., 2012, Modeling machining distortion using the finite element method: application to engine disk, in, pp. 40-46.
Knezevic, M., Jahedi, M., Korkolis, Y.P., Beyerlein, I.J., 2014. Material-based design of the extrusion of bimetallic tubes. Comput. Mater. Sci. 95, 63–73.
Knezevic, M., Carpenter, J.S., Lovato, M.L., McCabe, R.J., 2014. Deformation behavior of the cobalt-based superalloy Haynes 25: Experimental characterization and crystal plasticity modeling. Acta Mater. 63, 162–168.
Knezevic, M., Drach, B., Ardeljan, M., Beyerlein, I.J., 2014. Three dimensional predictions of grain scale plasticity and grain boundaries using crystal plasticity finite element models. Comput. Meth. Appl. Mech. Eng. 277, 239–259.
Knezevic, M., Zecevic, M., Beyerlein, I.J., Bingert, J.F., McCabe, R.J., 2015. Strain rate and temperature effects on the selection of primary and secondary slip and twinning systems in HCP Zr. Acta Mater. 88, 55–73.
Knezevic, M., Zecevic, M., Beyerlein, I.J., Lebensohn, R.A., 2016. A numerical procedure enabling accurate descriptions of strain rate-sensitive flow of polycrystals within crystal visco-plasticity theory. Comput. Meth. Appl. Mech. Eng. 308, 468–482.
Knezevic, M., Daymond, M.R., Beyerlein, I.J., 2016. Modeling discrete twin lamellae in a microstructural framework. Scr. Mater. 121, 84–88.
Koenigsmann, Z.W., Shankar, R., Fenton, R., 2016. Mechanical properties and microstructure design in repairing Mar-M 509 alloy turbine components. Proceedings of the 13th Intenational Symposium of Superalloys. Wiley Online Library, pp. 693–699.
Lashgari, S.M., Yari, H., Mahdavian, M., Ramezanzadeh, B., Bahlakeh, G., Ramezanzadeh, M., 2021. Application of nanoporous cobalt-based ZIF-67 metal-organic framework (MOF) for construction of an epoxy-composite coating with superior anti-corrosion properties. Corros. Sci. 178, 109099.
Lavrentev, F.F., 1980. The type of dislocation interaction as the factor determining work hardening. Mater. Sci. Eng. 46, 191–208.
Lebensohn, R.A., Needleman, A., 2016. Numerical implementation of non-local polycrystal plasticity using fast Fourier transforms. J. Mech. Phys. Solids 97, 333–351.
Lebensohn, R.A., Tomé, C., 1993. A self-consistent anisotropic approach for the simulation of plastic deformation and texture development of polycrystals: application to zirconium alloys. Acta Metal. Mater. 41, 2611–2624.
Lebensohn, R., Tomé, C., Castaneda, P.P., 2007. Self-consistent modelling of the mechanical behaviour of viscoplastic polycrystals incorporating intragranular field fluctuations. Philos. Mag. 87, 4287–4322.
Lebensohn, R.A., Kanjarla, A.K., Eisenlohr, P., 2012. An elasto-viscoplastic formulation based on fast Fourier transforms for the prediction of micromechanical fields in polycrystalline materials. Int. J. Plast. 32-33, 59–69.
Lebensohn, R.A., 2001. N-site modeling of a 3D viscoplastic polycrystal using fast Fourier transform. Acta Mater. 49, 2723–2737.
Li, Y., Chen, K., Narayan, R.L., Ramamurty, U., Wang, Y., Long, J., Tamura, N., Zhou, X., 2020. Multi-scale microstructural investigation of a laser 3D printed Ni-based superalloy. Addit. Manuf. 34, 101220.
R. Madec, B. Devincre, L. Kubin, T. Hoc, D.J.S. Rodney, The role of collinear interaction in dislocation-induced hardening. Science 301 (2003) 1879-1882.
Mecking, H., Kocks, U.F., 1981. Kinetics of flow and strain-hardening. Acta Metall. Mater. 29, 1865–1875.
Michel, J., Moulinec, H., Suquet, P., 2001. A computational scheme for linear and non-linear composites with arbitrary phase contrast. Int. J. Numer. Methods Eng. 52, 139–160.
Murr, L.E., Quinones, S.A., Gaytan, S.M., Lopez, M.I., Rodela, A., Martinez, E.Y., Hernandez, D.H., Martinez, E., Medina, F., Wicker, R.B., 2009. Microstructure and mechanical behavior of Ti-6Al-4V produced by rapid-layer manufacturing, for biomedical applications. J. Mech. Behav. Biomed. Mater. 2, 20–32.
Perini, M., Bosetti, P., Balc, N., 2020. Additive manufacturing for repairing: from damage identification and modeling to DLD. Rapid Prototyp. J. 26, 929–940. https://doi.org/10.1108/RPJ-03-2019-0090.

Safdar, S., Pinkerton, A.J., Li, L., Sheikh, M.A., Withers, P.J., 2013. An anisotropic enhanced thermal conductivity approach for modeling laser melt pools for Ni-base super alloys. Appl. Math. Model. 37, 1187–1195.
Santos, E.C., Shiomi, M., Osakada, K., Laoui, T., 2006. Rapid manufacturing of metal components by laser forming. Int. J. Mach. Tools Manuf. 46, 1459–1468.
Savage, D.J., Beyerlein, I.J., Knezevic, M., 2017. Coupled texture and non-Schmid effects on yield surfaces of body-centered cubic polycrystals predicted by a crystal plasticity finite element approach. Int. J. Solids Struct. 109, 22–32.
Sritharan, T., Chandel, R.S., 1997. Phenomena in interrupted tensile tests of heat treated aluminium alloy 6061. Acta Mater. 45, 3155–3161.
Tamura, R., Osada, T., Minagawa, K., Kohata, T., Hirosawa, M., Tsuda, K., Kawagishi, K., 2021. Machine learning-driven optimization in powder manufacturing of Ni-Co based superalloy. Mater. Des. 198, 109290.
Tao, P., Li, H., Huang, B., Hu, Q., Gong, S., Xu, Q., 2019. The crystal growth, intercellular spacing and microsegregation of selective laser melted Inconel 718 superalloy. Vacuum 159, 382–390.
Taylor, G.I., 1938. Plastic strain in metals. J. Inst. Metals 62, 307–324.
Thellaputta, G.R., Chandra, P.S., Rao, C., 2017. Machinability of nickel based superalloys: a review. Mater. Today Proc. 4, 3712–3721.
Uhlig, T., Weis, S., Wielage, B., Wagner, G., Schuberth, S., 2017. Properties of newly developed Co-based brazing fillers. Weld. World 61, 171–180.
Van Houtte, P., Li, S., Engler, O., 2004. Taylor-Type Homogenization Methods for Texture and Anisotropy. Continuum Scale Simulation of Engineering Materials: Fundamentals–Microstructures–Process Applications. Wiley-VCH Verlag GmbH & Co. KGaA, pp. 459–472.
Wang, S., Sun, Y., Hou, X., Cui, C., Sun, X., Zhou, Y., 2020. Investigation on microstructure and mechanical properties of a vacuum brazed joint of γ′-strengthened Co-based single crystal superalloy before and after the post-bond heat treatment. Vacuum 177, 109413.
Wen, W., Borodachenkova, M., Tomé, C.N., Vincze, G., Rauch, E.F., Barlat, F., Grácio, J. J., 2015. Mechanical behavior of Mg subjected to strain path changes: experiments and modeling. Int. J. Plast. 73, 171–183.
Whittenberger, J.D., 1981. Elevated-temperature mechanical-properties and residual tensile properties of 2 cast super-alloys and several nickel-base oxide dispersion strengthened alloys. Metall. Trans. A 12, 193–206.
Xu, Y., Li, W., Yang, X., Gu, Y., 2020. Evolution of grain structure, γ'precipitate and hardness in friction welding and post weld heat treatment of a new Ni-Fe based superalloy. Mater. Sci. Eng. A 788, 139596.
Zayed, A.I., 1998. A convolution and product theorem for the fractional Fourier transform. IEEE Signal Process. Lett. 5, 101–103.
Zecevic, M., Knezevic, M., 2015. A dislocation density based elasto-plastic self-consistent model for the prediction of cyclic deformation: Application to Al6022-T4. Int. J. Plast. 72, 200–217.
Zecevic, M., Knezevic, M., 2017. Modeling of sheet metal forming based on implicit embedding of the elasto-plastic self-consistent formulation in shell elements: application to cup drawing of AA6022-T4. JOM 69, 922–929.
Zecevic, M., Knezevic, M., 2018. Latent hardening within the elasto-plastic self-consistent polycrystal homogenization to enable the prediction of anisotropy of AA6022-T4 sheets. Int. J. Plast. 105, 141–163.
Zecevic, M., Knezevic, M., 2019. An implicit formulation of the elasto-plastic self-consistent polycrystal plasticity model and its implementation in implicit finite elements. Mech. Mater. 136, 103065.
Zecevic, M., Knezevic, M., Beyerlein, I.J., Tomé, C.N., 2015. An elasto-plastic self-consistent model with hardening based on dislocation density, twinning and de-twinning: application to strain path changes in HCP metals. Mater. Sci. Eng. A 638, 262–274.
Zecevic, M., McCabe, R.J., Knezevic, M., 2015. A new implementation of the spectral crystal plasticity framework in implicit finite elements. Mech. Mater. 84, 114–126.
Zecevic, M., McCabe, R.J., Knezevic, M., 2015. Spectral database solutions to elasto-viscoplasticity within finite elements: Application to a cobalt-based FCC superalloy. Int. J. Plast. 70, 151–165.
Zecevic, M., Korkolis, Y.P., Kuwabara, T., Knezevic, M., 2016. Dual-phase steel sheets under cyclic tension–compression to large strains: experiments and crystal plasticity modeling. J. Mech. Phys. Solids 96, 65–87.
Zecevic, M., Beyerlein, I.J., Knezevic, M., 2017. Coupling elasto-plastic self-consistent crystal plasticity and implicit finite elements: applications to compression, cyclic tension-compression, and bending to large strains. Int. J. Plast. 93, 187–211.
Zecevic, M., Lebensohn, R.A., McCabe, R.J., Knezevic, M., 2018. Modeling of intragranular misorientation and grain fragmentation in polycrystalline materials using the viscoplastic self-consistent formulation. Int. J. Plast. 109, 193–211.
Zecevic, M., Beyerlein, I.J., Knezevic, M., 2018. Activity of pyramidal I and II <c+a>slip in Mg alloys as revealed by texture development. J. Mech. Phys. Solids 111, 290–307.
Zecevic, M., Lebensohn, R.A., McCabe, R.J., Knezevic, M., 2019. Modeling recrystallization textures driven by intragranular fluctuations implemented in the viscoplastic self-consistent formulation. Acta Mater. 164, 530–546.
Zecevic, M., Knezevic, M., McWilliams, B., Lebensohn, R.A., 2020. Modeling of the thermo-mechanical response and texture evolution of WE43 Mg alloy in the dynamic recrystallization regime using a viscoplastic self-consistent formulation. Int. J. Plast. 130, 102705.
Zhang, P., Yuan, Y., Gu, Y., Yan, J., Dang, Y., Lu, J., Wang, J., 2020. Investigation on the tensile deformation mechanisms in a new Ni–Fe-base superalloy HT700T at 750°C. J. Alloy. Compd. 825, 154012.
Zhang, Y., Fu, H., Zhou, X., Zhang, Y., Dong, H., Xie, J., 2020. Microstructure evolution of multicomponent γ′-strengthened Co-based superalloy at 750°C and 1000°C with different Al and Ti contents. Metall. Mater. Trans. A 51, 1755–1770.
Zong, Y., Wu, K., 2017. Thermo hydrogen treatment for microstructure refinement and mechanical properties improvement of Ti-6Al-4V alloy. Mater. Sci. Eng. A 703, 430–437.